










# Role of Integrated Magnetics and Geology in Tracking and Exploring Complex Structures Controlling Gold Mineralization. Example from the Fawakheir-Atalla Gold Prospects, Eastern Desert, Egypt

MOHAMED MOSTAFA GOBASHY,<sup>1</sup>  ABDELMONEM ELDOUGDOU,<sup>2</sup>  MOHAMED ABDELWAHED,<sup>2</sup>   
MAHA ABDELAZEEM,<sup>3</sup>  YASSER ABD EL-RAHMAN,<sup>2</sup>  AHMED ABDELHALIM,<sup>2</sup>   
and SAID SAID<sup>2</sup> 

**Abstract**—Gold mineralisation is spatially and chronologically correlated with fault/shear zones in many of the world-class gold mines. Hence, the indirect exploration for Au mineralisation is linked with shearing and complex structures in many areas. Hence, in general, the need for a rapid, effective and new technology for gold exploration that reflects the structure set-up, shear zones, faults and related structural elements is crucial in the gold industry. In this article, we present an example of an integrated approach to gold exploration in the Fawakheir-Attala gold mining prospect in the eastern desert of Egypt. Remote sensing is used to test for rock differentiation; intensive field geological investigations were conducted along several traverses. Petrographic and geochemical analysis of selected samples confirmed Au content in some localities. Moreover, magnetic methods are used extensively (either aeromagnetic or measured land profiles) to investigate the magnetic signature of the different reported rock units and their relationship with gold occurrences and deposits. Normalised source strength transformation, magnitude magnetic transforms and subsurface modelling are used to explore the inherent relation between the surface and subsurface magnetic susceptibilities. The magnetic signature of the talc-carbonate rocks is determined. The gradational contact against the serpentinite is explained. Because three current Au mines are associated with contacts/fractures, the clear relation between the contacts/fractures and the magnetic data and the comparison with the contact occurrence density COD (heat) magnetic filtered map, the present analysis workflow can now be used to suggest new locations for Au occurrences.

**Keywords:** Magnetic tomography, Gold exploration, Fawakheir, Magnetics and geology, Heat map, Mineralisation.

## 1. Introduction

The Arabian-Nubian Shield is considered the largest Neoproterozoic gold resource on Earth (Johnson et al., 2017). The Eastern Desert of Egypt constitutes the northwestern extension of the Arabian-Nubian Shield. The Eastern Desert contains many gold occurrences that were mined since pre-dynastic (about 3000 BC) through the Pharaonic periods till the end of the Arab times (ca. 1350 AD) (Klemm et al., 2001). Gold exploitation in the Eastern Desert was documented by the Turin Papyrus. This papyrus is recognised as the oldest surviving geological map in the world (ca. 1150 BC) and shows the mined gold-bearing quartz veins and the gold-working settlements at the Fawakheir-Atalla area (Harrell & Brown, 1992).

An excellent example of the associated spatially and chronologically correlated fault/shear zones with gold mineralisation is in the Fawakheir-Atalla area. It is located in the central segment of the Eastern Desert. Throughout the central Eastern Desert, gold occurrences are commonly confined to extensive shear zones related to the NW-trending Najd Fault System (ca. 640–570 Ma), which cut the mafic-ultramafic ophiolitic assemblages (Zoheir et al., 2019). Gold mineralisation occurs also in structurally controlled quartz veins, which are often associated with late-orogenic granitic intrusions, especially where these intrusions are in contact with ophiolitic rocks (Klemm et al., 2001; Zoheir et al., 2019). Genetically, the gold and base metals were probably leached from

<sup>1</sup> Geophysics Department, Faculty of Science, Cairo University, Giza, Egypt. E-mail: Gobashy@sci.cu.edu.eg

<sup>2</sup> Geology Department, Faculty of Science, Cairo University, Giza, Egypt. E-mail: amaghawry@sci.cu.edu.eg; mawahed@sci.cu.edu.eg; yasser@sci.cu.edu.eg; ahmedabdelhalim@cu.edu.eg; szidan@sci.cu.edu.eg

<sup>3</sup> National Research Institute of Astronomy and Geophysics, Helwan, Egypt. E-mail: maazeem03@nriag.sci.eg

the ophiolitic serpentinite intruded by the granitic rocks (Abd El-Rahman et al., 2012; Harraz, 2001).

Although the Fawakheir-Atalla area hosts a potential World-class gold deposit (Helmy & Zoheir, 2015), limited studies have been conducted to trace the highly prospective rock units and structures for gold exploration and the associated shearing/fault zones. Data from satellite-based remote sensing systems are useful for both lithological mapping and mineral exploration (Sabins, 1999). Various remote sensing techniques have been used for mapping ophiolitic rocks, especially serpentinites, in the Eastern Desert of Egypt (e.g., Emam et al., 2016; Gad & Kusky, 2006; Qiu et al., 2006). Amer et al. (2010) used Advanced Spaceborne Thermal Emission and Reflection Radiometer (ASTER) data for lithological mapping of the area surrounding the Fawakheir area. In addition to lithological mapping, satellite remote sensing data were used for distinguishing the relationship among rock units, geological structures and gold mineralisation in the Eastern Desert of Egypt (e.g., Abu El-Leil et al., 2019; Ramadan et al., 2001; Salem et al., 2016). Abu El-Magd et al. (2015) used the ASTER images to map the lithology, structural patterns and alteration zones related to the gold mineralisation of the Fawakheir area. Unlike remote sensing, magnetic data are a useful tool for identifying subsurface geological features, such as geological structures, which are important in mineral exploration (Dufrechou et al., 2015; Holden et al., 2008; Yang et al., 2021; Zhu & Lu, 2021). Particularly, it is used as a reconnaissance technique and has many geological applications, including geological mapping of probable places with buried igneous bodies that are frequently associated with mineralisation, recognising supra-basement features and calculating the thickness of sedimentary cover (Abdelazeem et al., 2013, 2021) in petroleum exploration and modelling of geothermal and groundwater resources; analysis of the tectonic structure, detection of intra-basement faults and uplifts, basin modelling, structural geometry (Abdelazeem et al., 2014; Al-Garni & Gobashy, 2010; El-Sawy et al., 2018; Gobashy et al., 2021b), finding buried objects like pipes, drums and unexploded bombs is made easier by enabling visualisation of the geological structure of the upper crust, particularly

the spatial geometry of lithological units and the presence of folds and faults and unexploded ordnance (Abdelazeem & Gobashy, 2016; Nazih et al., 2022). Additionally, it is an efficient tool in mineral exploration (EldougDoug et al., 2023; Abdelhalim et al., 2020; Abdelazeem et al., 2019; Aboelkhair et al., 2020; Al-Garni & Gobashy, 2010; Abdelrahman & Gobashy, 2019; El-Sawy et al., 2018; Groves et al., 1984, and, Gobashy et al., 2020a, 2020b Gobashy et al., 2021a, 2021b, and Gobashy et al., 2022; Rehman et al., 2019) where it adds a third dimension of exploration and increases the Au exploration opportunities by revealing the subsurface concentrations of mineralised zones including Au.

Integrating remote sensing and magnetic data is successfully used to define the prospective gold mineralisation areas in the Eastern Desert of Egypt (e.g., Eldosouky et al., 2020; ElGalladi et al., 2022). Gobashy et al. (2021b) integrated remote sensing data and aeromagnetic technique to predict the areas of high gold potentiality within the ophiolitic serpentinite in the Barramiya area in the Eastern Desert of Egypt. Elkhateeb and Abdellatif (2018) used both aeromagnetic and radiometric regional surveys to locate probable gold mineralisation zones in the Atalla-Fawakheir area.

Due to the lack of information about the relation between the subsurface distribution of magnetic susceptibilities and gold mineralisation in general, and in particular in the Fawakheir-Attala high-potential gold mineralisation zone, the present work is initiated to help identify the surface and subsurface potential occurrence of gold mineralisation and assisting in mapping the structural and lithological features. The available aeromagnetic data were processed and reduced to the pole (RTP), and various filters, such as normalised source strength (NSS), analytic signal (AS), Euler's deconvolution and tilt angle, were applied. The delineation of potential gold deposits and the identification of geological discontinuities (dykes, faults and shear zones) that serve as conduits for mineralising fluids are also accomplished using a variety of grid analysis techniques. The West Fawakheir-Attalla region will be used to test the aforementioned approach. In other words, this research is designed to determine (search for) different types of gold mineralisation other than the

well-known gold quartz veins (QVs) associated with diorite/granodiorite intrusion in the Fawakheir gold mine. A scheme is presented to find new mineralisation zones associated with hydrothermally altered ophiolitic ultramafic rocks utilising integrated geology with subsurface magnetic susceptibility inversion using a regularised algorithm. Figure 1 shows the workflow used in this study. Three phases are introduced. The first is for data collection, preparation and Dbase building. This phase ends up with the production of a geological map. The second is for data analysis and filtering. It includes aeromagnetic basic

filtering and structural, petrographic and geochemical analysis. The third phase is result integration and interpretation and gold potential zone identifications based on the proposed workflow.

## 2. Geological Setting and Remote Sensing

El Fawakheir area lies at the southern central part of the Golden Triangle and is delimited by latitudes 25° 54' 37.42" to 26° 09' 22.96" N and longitudes 33° 30' 01.94" to 33° 40' 20.36" E (Fig. 2a). The

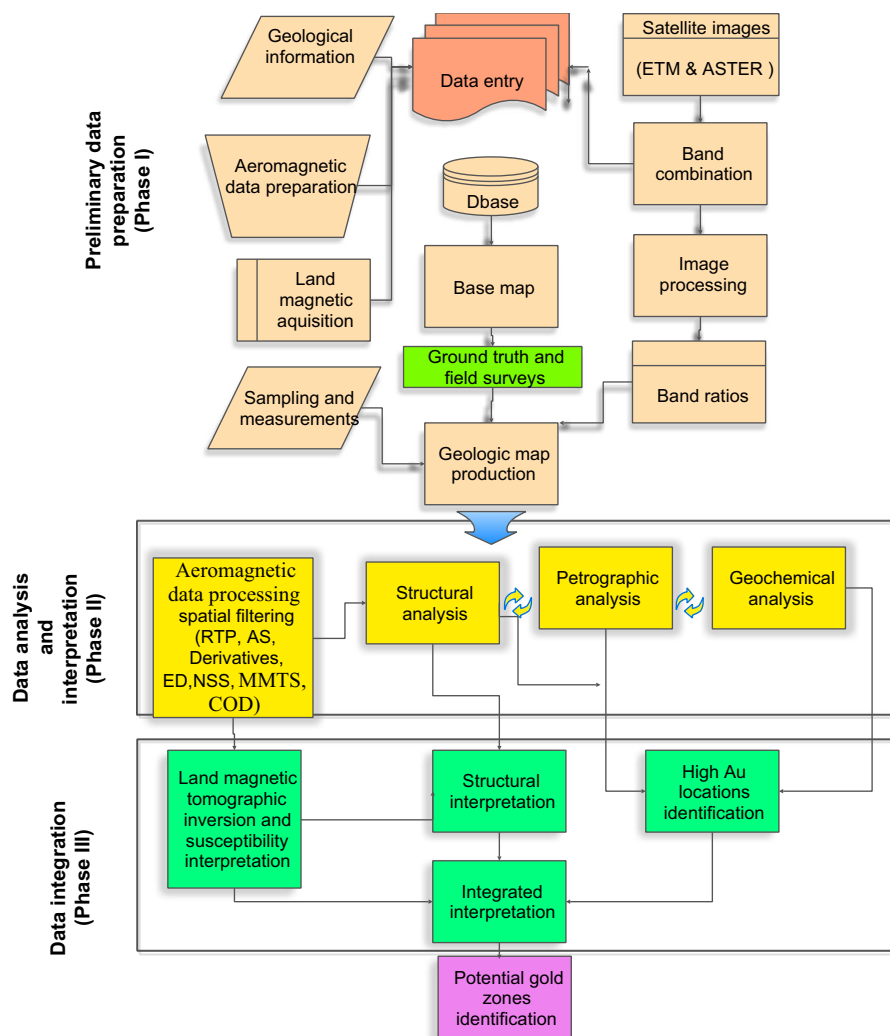


Figure 1  
a Flowchart describing the proposed scheme used in this study

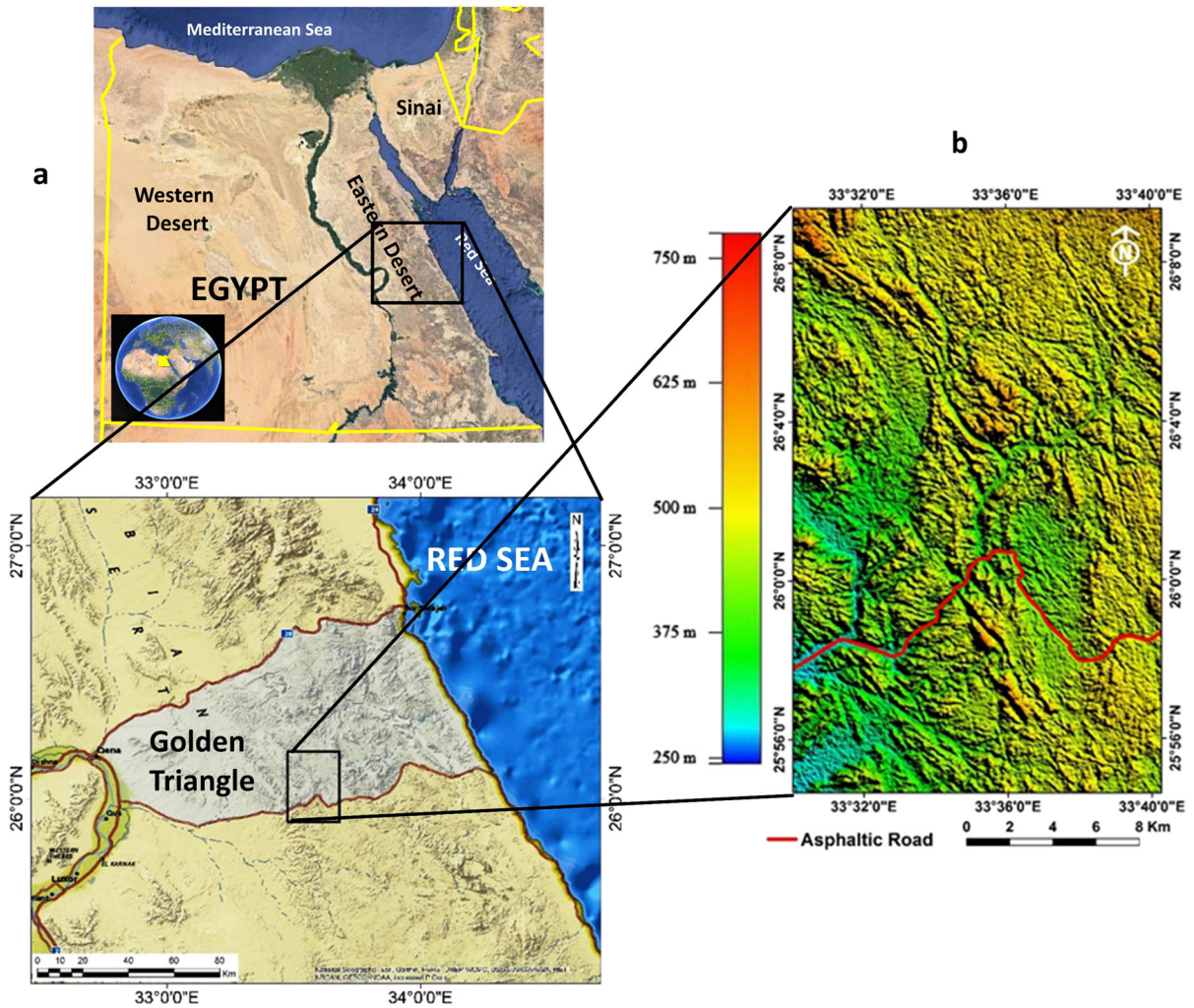


Figure 2

**a** Location map of the golden triangle and Fawakheir area. **b** Shaded relief model of the study area. Aster GDEM data, 30 m resolution

area is easily accessible from Quseir City on the Red Sea coast or from Qena Governorate in the Nile Valley where it is crossed by the Quseir-Qift road (Fig. 2). The study area is characterised by rugged topography and narrow valleys reaching an elevation up to 755 m above sea level at its northern parts (Fig. 2b).

### 3. Methodology and Interpretation of Remote Sensing Data

The extensive use of ASTER and Landsat-8 data (worldwide and particularly in Egypt) became an

important issue to cover remote sites of basement complexes and detect the most promising ore spots (Abdeen et al., 2001; Aboelkhair et al., 2010, 2020; Abrams et al., 2002; Abuelella et al., 2021; Gobashy et al., 2021b; Kalinowski & Oliver, 2004; Mars & Rowan, 2006; Salem et al. (2018); Seleem et al., 2020). Geological mapping of the Fawakheir-Atalla area in previous studies has been reviewed (e.g., Abd El-Wahed, 2009; Abd El Monsef, 2020; Akaad & Noweir, 1980; Conoco Maps, 1987; El-Magd, et al., 2014; Zoheir, et al., 2015, 2018) and a new geological map is constructed in this study based on detailed satellite image interpretation and field check. Moreover, image enhancement techniques are applied

through the ENVI-V5 software using RGB band combination images and mathematical rationing of multispectral Landsat-8 and ASTER data.

#### 4. Materials and Methods

RGB band combination and ratio images are used in the current study and proved their efficiency in the lithological discrimination of the serpentines and associated rock units. The following Landsat-8 and Aster data scenes are used to discriminate the rock units and geological contacts:

- Landsat-8, scene ID = LC08\_L1TP\_174042\_20180616\_20180703\_01\_T1, acquired at 2018/06/16.
- Aster data, scene ID = AST\_L1T\_00303262006083536\_20150513171833\_56433, acquired at 2006/03/26.
- Aster data, scene ID = AST\_L1T\_00304062001084023\_20150415125738\_81735, acquired at 2001/04/06.

Landsat-8 data consist of 11 bands differentiated into 8 bands of 30-m resolution (visible, NIR, SWIR and cirrus bands), one panchromatic band of 15-m resolution and two thermal infrared bands of 100-m resolution. Aster data consist of 14 bands differentiated into three bands of 15-m spatial resolution (visible and near infrared, VNIR), 6 bands with 30-m spatial resolution (SWIR), 5 bands with 90-m spatial resolution (TIR) and an additional backward telescope for stereo. Landsat-8 and Aster data used are all of resolutions up to 15 m/pixel that produce an image of a scale reaching up to 1:40,000 without any remarkable pixilation and are suitable for the present work. Different remote sensing techniques are applied to construct the base maps of the study area. Processing of satellite data has been done through the following techniques:

1. Layer stacking of the different bands in the image.
2. Mosaicking of images where needed in the Aster data.
3. Sub-setting of images to get the exact area needed.

4. Construction of False Color Composite (FCC) images using the band combination and band rationing techniques to obtain the best lithological discrimination and identify the ultramafic bodies.
5. Enhancement and merging techniques are used during the processing. The UTM projection (WGS84 datum, zone 36N) is also utilised for the produced images.

Registered high-resolution satellite images, e.g., Quick birds from Google Earth and Bing Esri maps, were used to refine the mapping of geological structures, e.g., folds, thrust faults and strike-slip faults. The remote sensing data were validated during the seasons of fieldwork through the accurate check of the different structures and rock types and their contacts along many field stations.

Results show that the RGB band combinations (7, 5, 3) and (7, 3, 1) for Landsat-8 and Aster data, respectively, are constructed to test for rock differentiation (Fig. 3. a and b). The serpentine appears in dark green, while there are some difficulties differentiating other rock units in many parts of the studied area.

Accordingly, the band rationing of both Landsat-8 and Aster images is carried out after multiple mathematical indices to finite the rock units carefully (Abdeen et al., 2001; Gad & Raef, 2012). The most suitable band ratios examined are 6/7, 6/2, 4/2 and 4/6, 4/1, and 2/1 in RGB for Landsat 8 and Aster data, respectively (Fig. 4a and b), in which the serpentinite appears in bright red and the metavolcanics are in dark red, and the other rock units are considerably differentiated.

Better differentiation of rock unit contacts is found in the band ratios 7/6, 6/2 and 4/2 of Landsat-8 data (Fig. 5a), in which the serpentinite has a brownish black and dark blue colour, the basic metavolcanics are in bright orange, the acidic metavolcanics are in light blue, the Hammamat sediments are in dark red, and the post-Hammamat felsite is in bright green. The rock units are classified into 12 units according to their characteristic reflectance in the satellite images, geological setting and petrography, as shown in Fig. 5b.

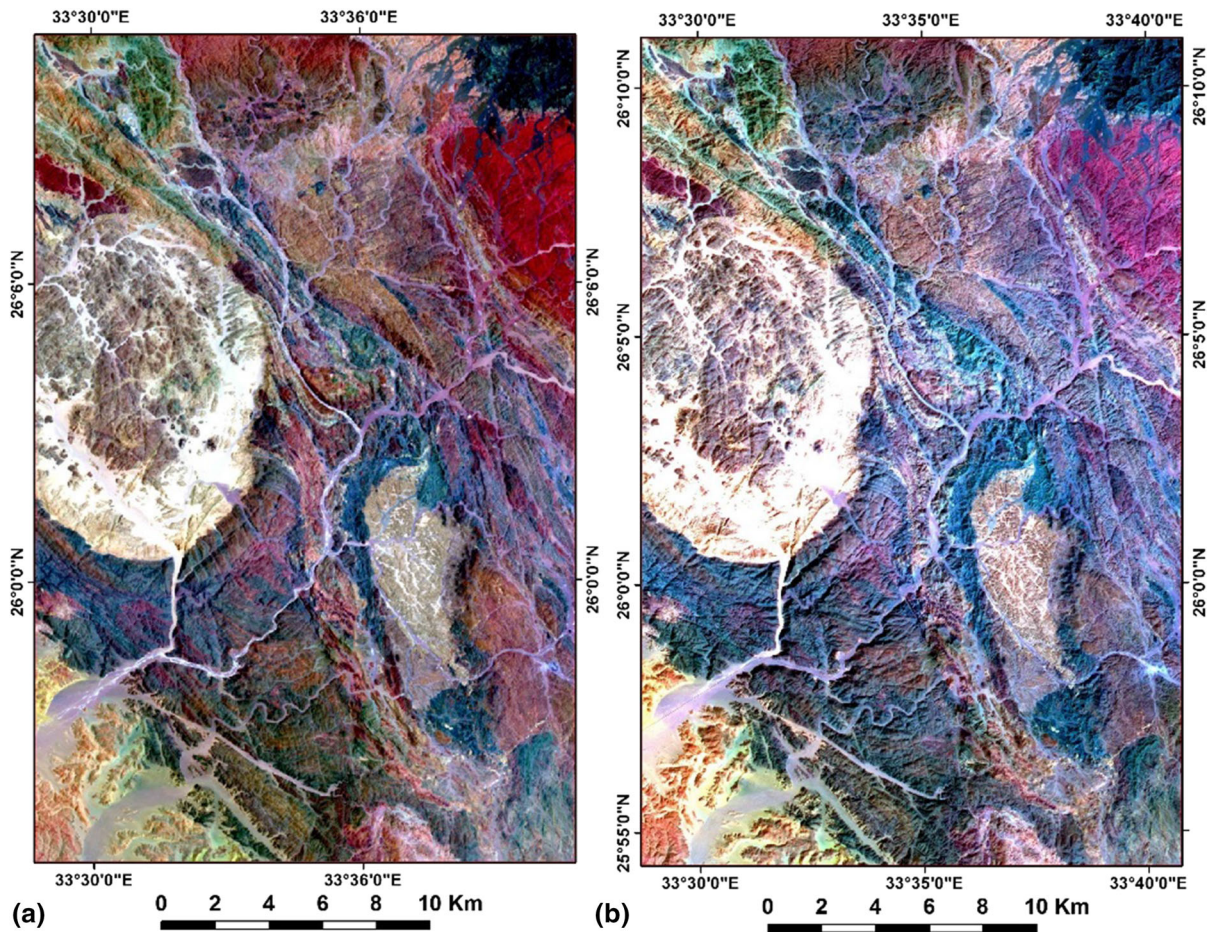


Figure 3

**a** Landsat-8 image of Fawakheir area of band combination 7,5,3 for RGB. **b** Aster image of Fawakheir area of band combination 7,3,1 for RGB; both show serpentinites in dark green colour and basic metavolcanic in blood red

#### 4.1. Geological Setting

Several NE- and WNW-oriented traverses were followed during a detailed field investigation of the Fawakheir area to achieve the aim of the study. These traverses were chosen based on the preliminary mapping of the rock units and main structure elements detected through different remote sensing analyses and reconnaissance fieldwork. The fieldwork is focused on sampling the ultramafic rocks and their alterations and measuring structural attitudes. Each field spot was recorded using GPS and all the measured structural data was geometrically analysed. All previous data were listed in an ArcGIS database and were manipulated to construct the final

geological map. The presented map (Fig. 6a) shows two Litho-tectonic sequences.

- (1) Syn-orogenic sequence including highly sheared low-grade metamorphosed ophiolitic mélangé and island arc metavolcanic, which were intruded by syn-orogenic granodiorite.
- (2) Post-orogenic sequence including Hammamat molasse sediments, post-Hammamat felsites and post-orogenic granites.

The study area includes three old gold mines; Fawakheir and El Sid gold mines are within the syn-orogenic metavolcanic at the central and southwestern parts of the mapped area, and the Atalla mine is within the post-orogenic granite at the extreme NW

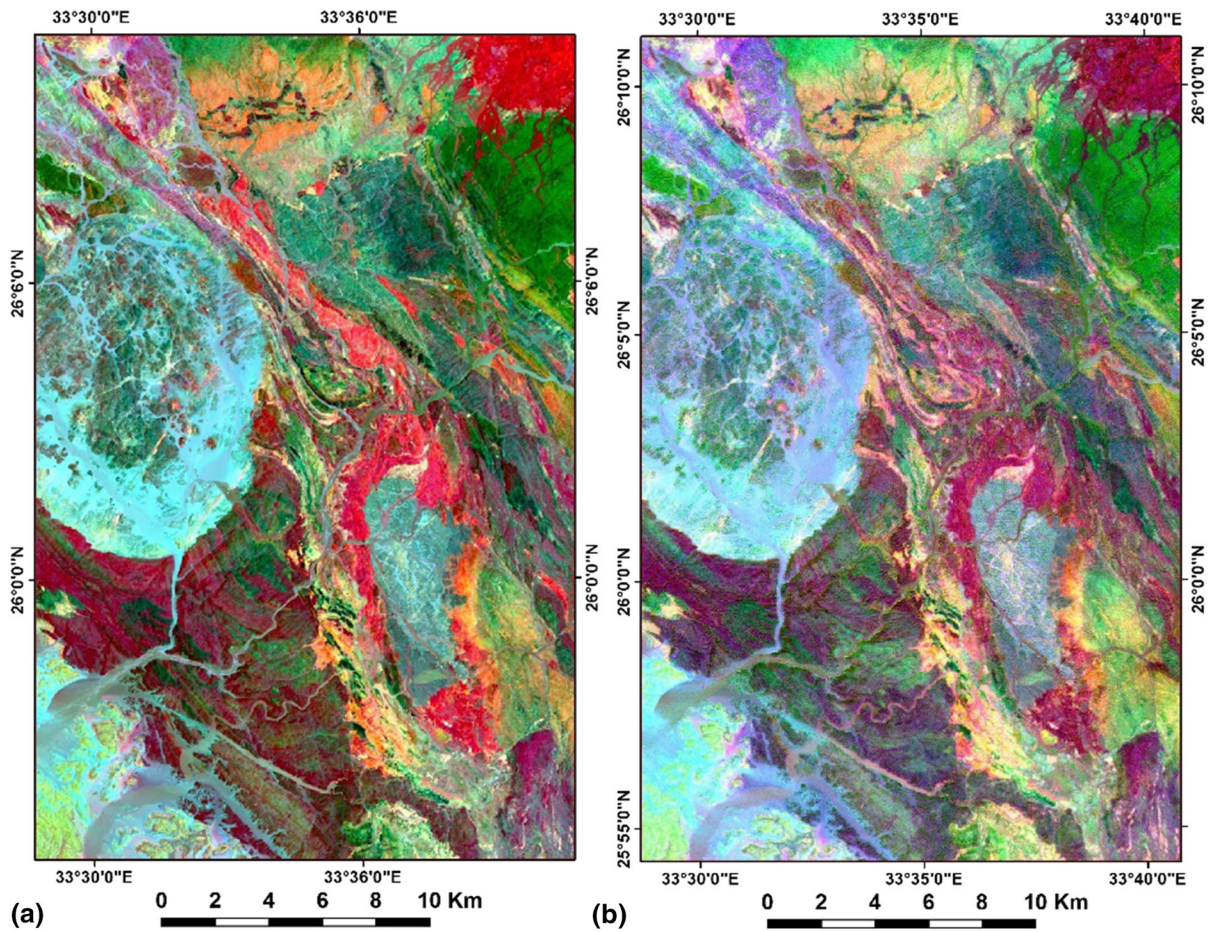


Figure 4

**a** Colour ratio composite image applied to the study area. **b** Landsat-8 image of band ratio 6/7, 6/2, and 4/2 in RGB. **b** Aster image of band ratio 4/6, 4/1 and 2/1 in RGB

part. Recently, the area was assigned to an international gold exploration and production company (SMW Gold Co.).

### 1. Syn-orogenic sequence

This succession was subjected to low-grade metamorphism under green-schist facies conditions. Metagabbro and serpentinites and their related rocks (such as talc carbonates and listwanite) are the most common rock types of ophiolites in the study area. They are best exposed and distributed in an NW-oriented belt along the Wadi Atalla shear zone and Wadi El-Sid at the NW, central and SW parts of the area (Fig. 6a). Along the Atalla shear zone, the

ophiolites are represented as elongated lenses and sheets of variable sizes trending in the NNW-SSE direction and bounded by a mélangé matrix of sheared metavolcanic and metasediments. The ultramafic lenses include serpentines and talc-carbonate thrust slices (Fig. 7c).

Basic and intermediate arc metavolcanic blocks of andesitic basalt and basaltic composition are mapped along the northwestern part of the Atalla shear zone and the NE and E parts of the mapped area. Several thrust sheets of metavolcanic and metagabbro are thrust westward above ultramafic succession (Fig. 7a). The ultramafic rocks in the Atalla-Fawakhier area mainly represent massive serpentinite, which

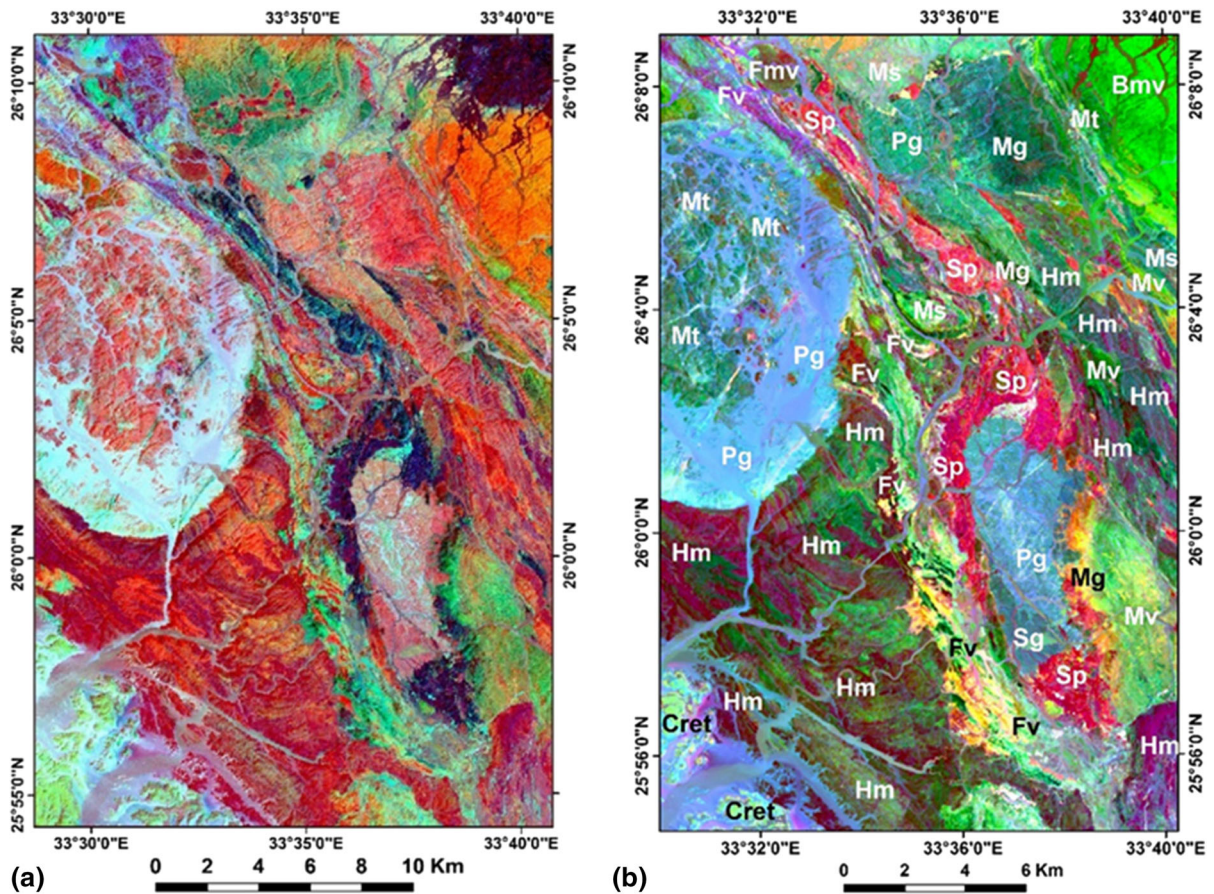


Figure 5

**a** Landsat-8 image of the study area of band ratio 7/6, 6/2 and 4/2 for RGB. **b** Landsat-8 image of Fawakheir area of band ratio 7/6, 6/2, 4/2 for RGB. *Mt* Medium to high-grade metamorphic rocks, *S* serpentinite, *Mg* Metagabbro, *Mv* metavolcanics undifferentiated, *Mvb* basic metavolcanics, *Mva* intermediate to acidic metavolcanics, *Ms* metasediments, *Sg* Syn-orogenic granite, *Hm* Hammamat group, *Fv* post-Hammamat felsites, *Pg* post-orogenic granite, *Crt* Cretaceous sediments

is composed of antigorite and chrysotile, which exhibit bastite (Fig. 8a) and mesh textures, and it encloses many chromite crystals. The chromite is variably replaced by ferritchromite, especially on their rims and along the fractures in the cataclased crystals (Fig. 8b). Magnetite is present also in the serpentinite of the Atalla-Fawakheir area. Two varieties of magnetite are recorded. The first variety is primary magnetite, which is represented by fine- to medium-grained euhedral to subhedral crystals disseminated variably in the serpentinite (Fig. 8c). The second variety is represented by secondary magnetite,

which forms skeletal crystals defining the cleavage planes of altered pyroxene (Fig. 8b) and extends along the fracture of the serpentinitised olivine (Fig. 8d). The magnetite, in particular, is of prime importance when defining the large magnetic anomalies in the study area. The sheared serpentinite is transformed into buff-coloured listvenite, which is composed of elongated carbonate- and silica-rich bands (Fig. 8e). Listvenite encloses relics of brecciated chromite that are intensively carbonatised (Fig. 8f). Presence of chromite and ferritchromite in serpentinites resulted in their high magnetic anomaly



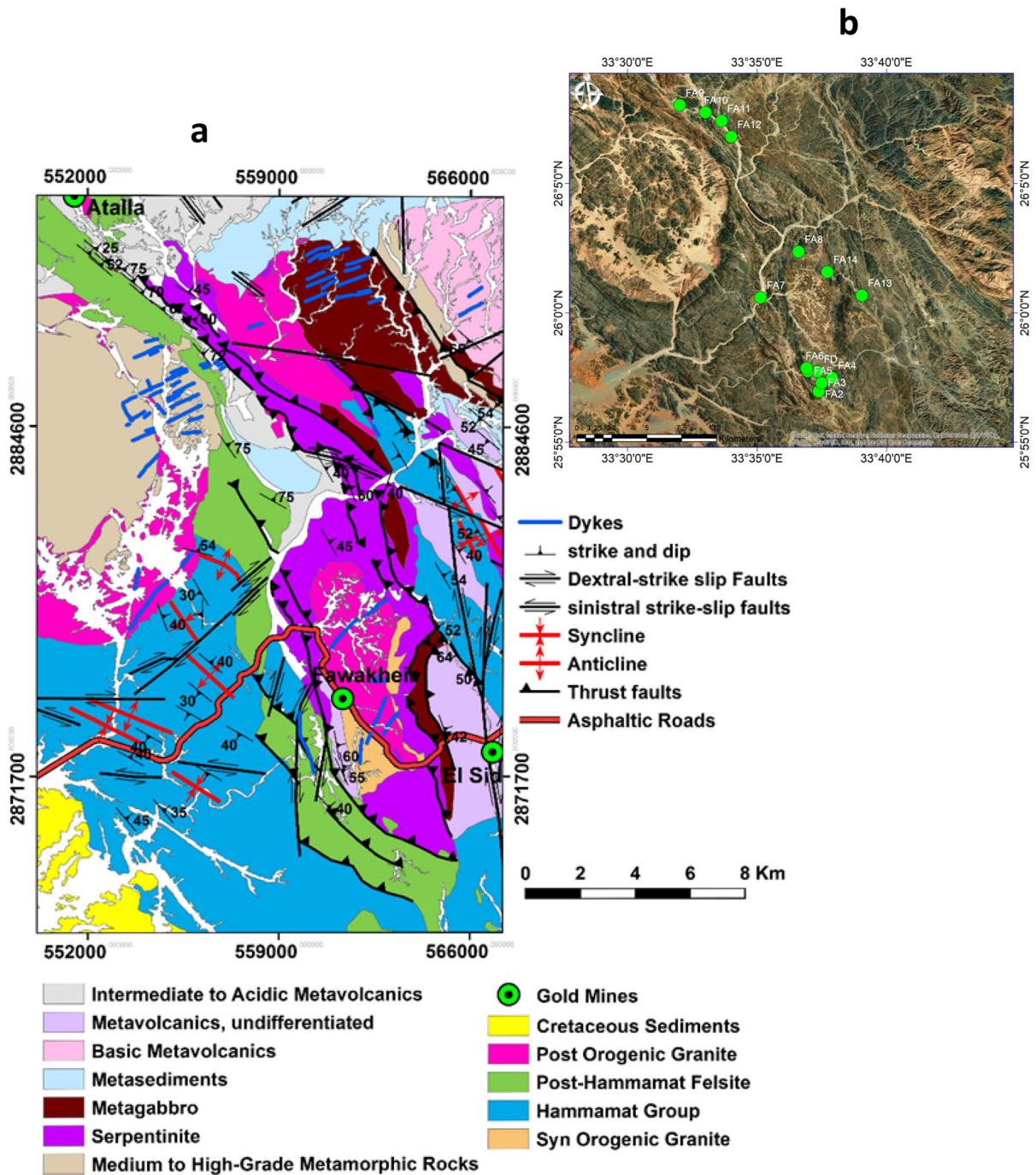


Figure 6

a Geological map of the Atalla-Fwakhier area and b locations of geological rock samples used for petrophysical and geochemical analysis

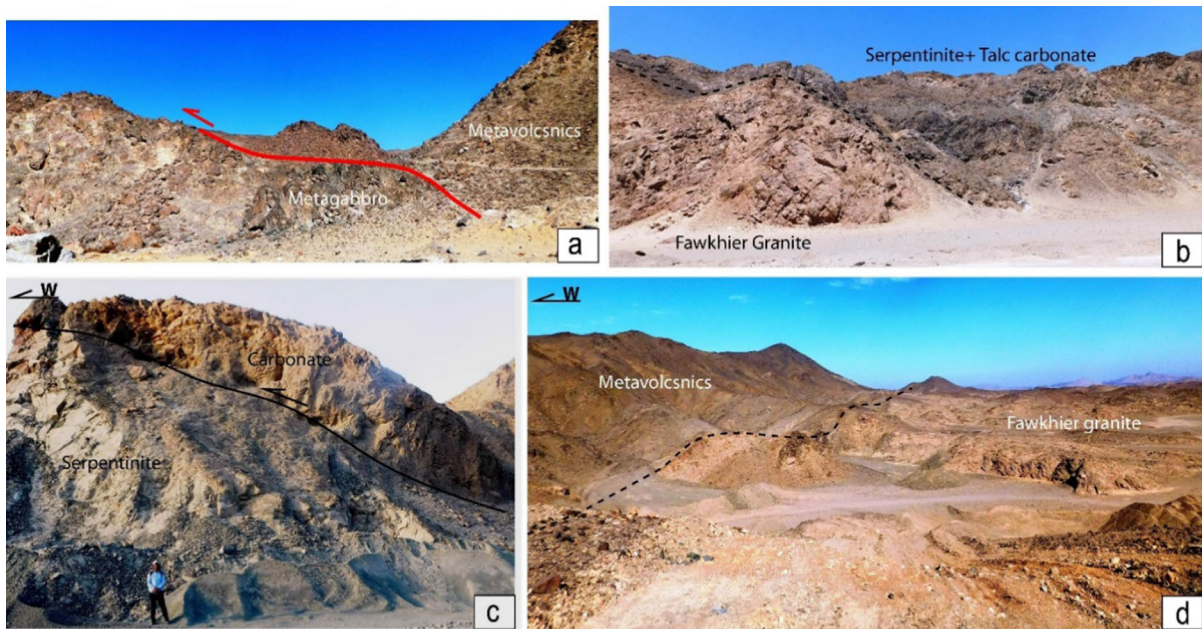


Figure 7

**a** Island arc metavolcanics thrust over ophiolitic metagabbro, **b** contact between Fwakhier granite and the ultramafic rocks, **c** carbonate thrust westward over serpentinite north of Fwakhier pluton and **d** metavolcanic is in contact with Fwakhier granite southwest of Fwakhier pluton

compared to other rock units exposed in the area, but their structurally controlled alteration to listvenite and in some talc carbonate (Fig. 7c) decreases their magnetic susceptibility.

## 2. Post-orogenic sequence

Hammamat molasse sediments form NW-trending strips in the west and east of the study area. They are composed mainly of deformed conglomerates and greywackes that are in thrust or unconformity contacts against the surrounding ophiolitic mélangé and arc metavolcanic. Conglomerates consist mainly of poorly sorted gravel-sized clasts that constitute mainly lithic fragments of basic metavolcanics, serpentinites, metagabbro and alkali granite.

## 3. Granitoid intrusions

Two different post-orogenic granitic intrusions were mapped in the study area; the Um had granite and Fwakhier granite. Um Had granite is a circular pluton exposed at the western part of the area, composed of alkali granite intruding the Hammamat sediments, and has roof pendants of medium-grade metamorphosed sediments.

Fwakhier granite occupies the southwest corner of the mapped area along the entrance of Wadi Hammamat. It is surrounded by ophiolitic mélangé along its northeastern and northwestern margins (Figs. 6 and 7b) and covered by metavolcanics along its southwestern margin (Fig. 7d).

Geochemically, five selected whole-rock samples (Fig. 6b) were analysed by x-ray fluorescence (XRF) for major and trace element contents and by fire assay for their gold content (Table 1). The analyses were conducted in the central laboratories of the Egyptian Mineral Resource Authority (EMRA). The samples comprise three serpentinite samples and two talc-carbonate samples. One of these talc-carbonate samples contains tremolite laths. Silica contents of serpentinite range from 39.72 to 42.62 wt%, and their MgO contents range from 30.62 to 37.25 wt%. The soapstone samples are characterised by lower MgO (22.37 wt%) and SiO<sub>2</sub> (36.81 wt%) contents compared to serpentinite. The occurrence of carbonate, which is dominantly magnesite, is manifested by high LOI values in soapstone (26.36 wt%) compared to serpentinite (13.02–13.91 wt%). The occurrence of tremolite is reflected in the high CaO content (13.12

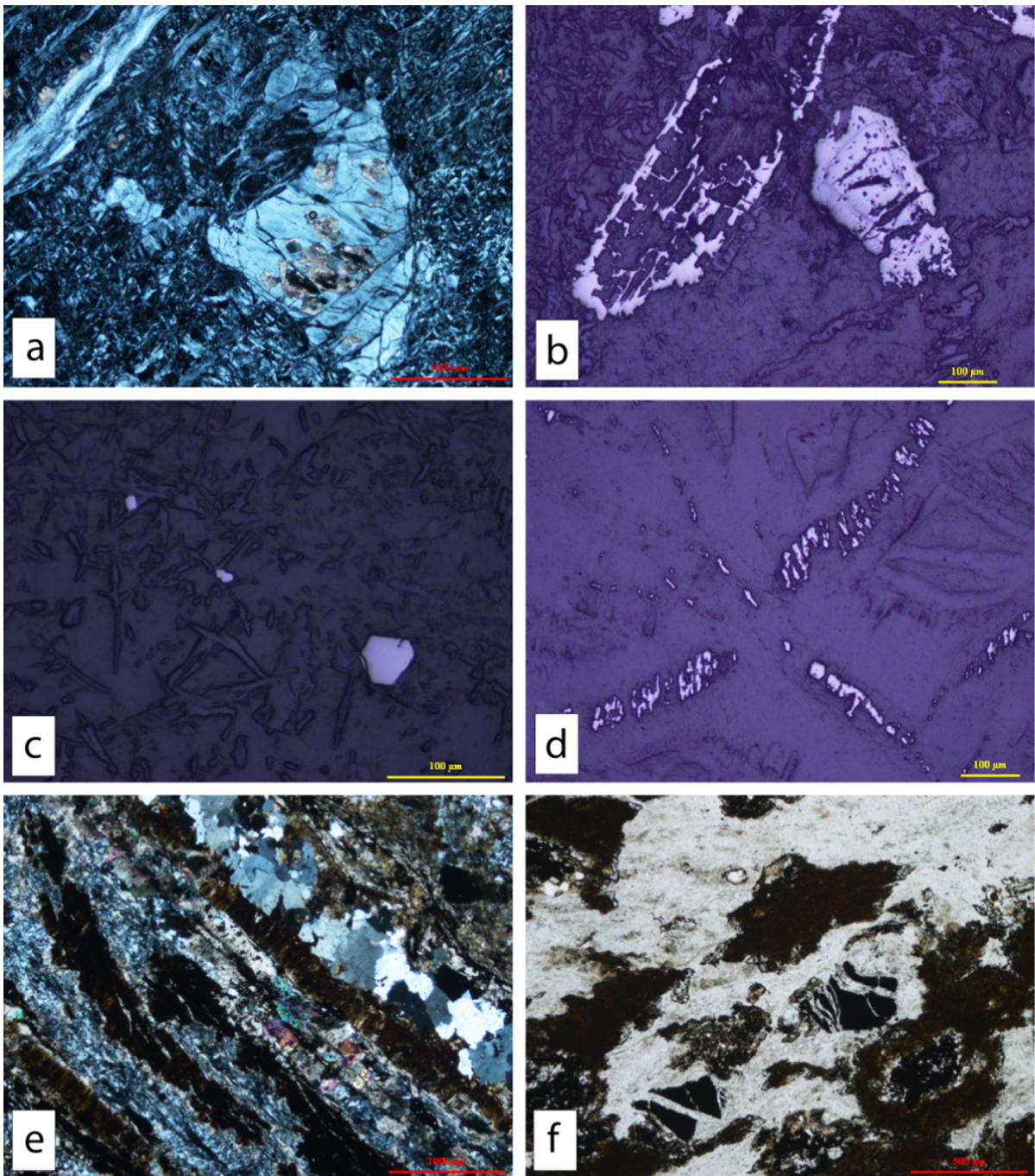


Figure 8

**a** Large serpentine after pyroxene in association with carbonate (yellow arrows) embedded in fine-grained serpentine matrix dissected by serpentine veinlets (PPL). **b** Skeletal magnetite defining the crystal boundaries and cleavage of a ghost pyroxene crystal on the left close to a fractured chrome-spinel crystal on the right showing alteration to ferritchromite (RL). **c** Euhedral magnetite disseminations in serpentinite (RL). **d** Magnetite aligned along the fractures of extensively serpentinised olivine crystal (RL). **e** Banded listvenite invaded by concordant quartz vein (XPL). **f** Brecciated relict chromite crystals, which are carbonatized along the rim (PPL). PPL plane-polarised light, XPL crossed-polarised light, RL reflected light

Table 1

Major and trace element compositions and gold analyses of representative samples from the Fawakhir-Atalla area (bdl: below detection limit)

Area	Fawakhir Atalla				
	FA1	FA3	FA14	C3	C4
Rock type	Serpentinite	Serpentinite	Serpentinite	Soapstone	Soapstone
Au ppm	0.3	0.5	9.5	1.6	5
SiO <sub>2</sub> wt%	42.62	41.38	39.72	36.81	42.44
TiO <sub>2</sub>	0.04	0.04	0.03	0.03	0.03
Al <sub>2</sub> O <sub>3</sub>	< 0.01	< 0.01	< 0.01	< 0.01	< 0.01
Fe <sub>2</sub> O <sub>3</sub>	9.87	11.8	8.49	9.61	7.26
MnO	0.15	0.17	0.07	0.2	0.14
MgO	30.62	30.87	37.25	22.37	18.49
CaO	2.4	1.85	0.93	4.29	13.12
Na <sub>2</sub> O	< 0.01	< 0.01	< 0.01	< 0.01	< 0.01
K <sub>2</sub> O	< 0.01	< 0.01	< 0.01	< 0.01	< 0.01
P <sub>2</sub> O <sub>5</sub>	< 0.01	< 0.01	< 0.01	< 0.01	< 0.01
Cl	< 0.01	< 0.01	< 0.01	< 0.01	< 0.01
SO <sub>3</sub>	0.08	0.2	0.18	0.04	0.14
F	< 0.01	< 0.01	< 0.01	< 0.01	< 0.01
LOI	13.91	13.4	13.02	26.36	18.08
Total	99.69	99.71	99.69	99.71	99.70
V ppm	25	37	9	12	23
Cr	2880	2310	1960	1179	1516
Co	113	122	124	95	75
Ni	2734	2663	3126	1790	1888
Cu	7	63	< 2	3	5
Zn	44	29	37	27	31
Sr	75	61	39	140	143
Zr	18	17	17	22	23
Nb	2	2	2	< 2	3
Ba	< 2	29	23	< 2	< 2
La	2	< 2	< 2	2	< 2
Pb	11	42	< 2	122	42
Th	2	< 2	< 2	< 2	< 2
U	< 2	< 2	< 2	< 2	2

wt%) of the C4 sample compared to the talc carbonate (4.29 wt%) and serpentinite, which exhibits the lowest CaO contents (0.93–2.4 wt%). The serpentinite exhibits slightly higher Cr (1960–2880 ppm), Ni (2663–3126 ppm) and Co (113–124 ppm) contents compared to the carbonated samples (1179–1516 ppm, 1790–1888 ppm, 75–97 ppm, respectively). Contrarily, Sr contents of the soapstone (140–143 ppm) are higher than those of serpentinite (39–75 ppm). Two of the serpentinite samples contain 0.3 and 0.5 ppm gold, which are less than in the carbonatised samples (1.6 and 5 ppm). The serpentinite sample FA14 contains exceptionally high gold

content (9.5 ppm). This sample also shows the highest Ni content (3126 ppm) and MgO/SiO<sub>2</sub> ratio (0.94) compared to the analysed rocks from the Golden Triangle.

#### 4.2. Structural Setting

##### 1. Foliation and lineation

Two generations of foliation have been recognised in the study area. The oldest one (S1) is pervasive in the ophiolite sequence and metavolcanic and is mainly represented by mylonitic fabric in the Atalla shear zone and along thrust planes.

## 2. Folds

Several NW folds were recorded in the Atalla shear zone and WNW folds were mapped in the Hammamat sediments (Fig. 6a). Mesoscopic overturned and tight upright folds of NW trends have been recognised along the Atalla shear zone affecting the ophiolite mélangé. Upright open to gentle folds with WNW–ESE steeply inclined axial planes and folding axes that plunge at low to moderate angles towards the WNW were mapped in the molasse sediments in the southwestern part of the study area (Fig. 6a).

## 3. Shear zone

The study area is marked by an NW-oriented high-strain zone known as the Atalla shear zone (ASZ). ASZ is defined by an NW-oriented steeply dipping mylonitic foliation (Fig. 8). Mylonites from the Atalla shear zone show great variation in the lithological composition and degree of deformation.

## 4. Faults

The study area is highly disrupted by faulting thrust, strike-slip and normal displacement. Thrust faults mainly strike in NW–SE to N-S direction, dipping generally towards NE, except in the north-eastern part of the study area where thrust faults dip to the SW. They are represented by imbricated thrust sheets that are distributed throughout the study area and mark the tectonic boundaries between the

different thrust sheets in Atalla succession as well as surrounding ophiolitic mélangé (Fig. 6a).

The structural framework of the Fawakheir area is the result of four deformational phases. The oldest is a compressional ductile deformation resulting in folds, thrust faults, schistosity and mylonitic foliation in the ophiolitic mélangé and arc metavolcanics of the synorogenic rock sequence. The second is a shear brittle deformation represented by dextral and sinistral conjugate strike-slip faulting, while the third is an extensional brittle deformation represented by normal faulting affecting older structural elements. The third phase of deformation is represented by extensional structures including NE–SW normal faults and joints, probably associated with the exhumation process of the Meatiq dome that lies just east of the study area, and associated with the development of Hammamat sediments basins. The fourth deformation phase resulted in the formation of NW-oriented folds and thrusts, foliation and lineation in the Hammamat group.

### 4.3. Magnetic Data Processing

The Western Geophysical Company of America carried out a survey (area II) of the CED and SED, Egypt, and retrieved the total magnetic intensity (TMI) map from the original magnetic anomaly map, CED, Egypt. The Egyptian General Petroleum Corporation (EGPC) completed this study in 1983. The necessary parameters for a magnetic survey are displayed in Table 2. The maps that covered the study area were re-digitised, edited and assembled in compliance with the required technical standards. A simple Gaussian filter was used to smooth a total of 163,677 data points. Figure 9a displays the generated preliminary TMI map. To consider the survey terrain clearance, the map is continued downward for 120 m. The magnetic intensity varies noticeably over some zones, which suggests variations in the lithology or basement structure. Using the map, we were able to estimate the magnetic relief to be around 1530 nT.

We generated the RTP magnetic anomaly map in the Fourier domain to reduce the magnetic field's skewness (Fig. 9b). The inclination and declination of the field were defined using estimations from the IGRF (International Geomagnetic Reference Field) at

Table 2

<i>Aeromagnetic survey parameters, Eastern desert, Area II, Egypt</i>	
Magnetometer	Varian VIW 2321G4 Single-Cell Cesium Vapor
Altitude	120 m (394 feet) terrain clearance
Flight line spacing:	Traverse = 1.0 KMS, tie = 10.0 KMS
Flight line direction	Traverse = 45_/225, tie = 135_/315_
Total magnetic field intensity(average)	42, 425 gamma
Central declination	1.9° East
Central inclination	32.8° North

Egyptian General Petroleum Corporation, Aero Service, 1983, 1984a, b. Interpretation report, airborne gamma-ray spectrometer and magnetometer survey of the eastern desert of Egypt.

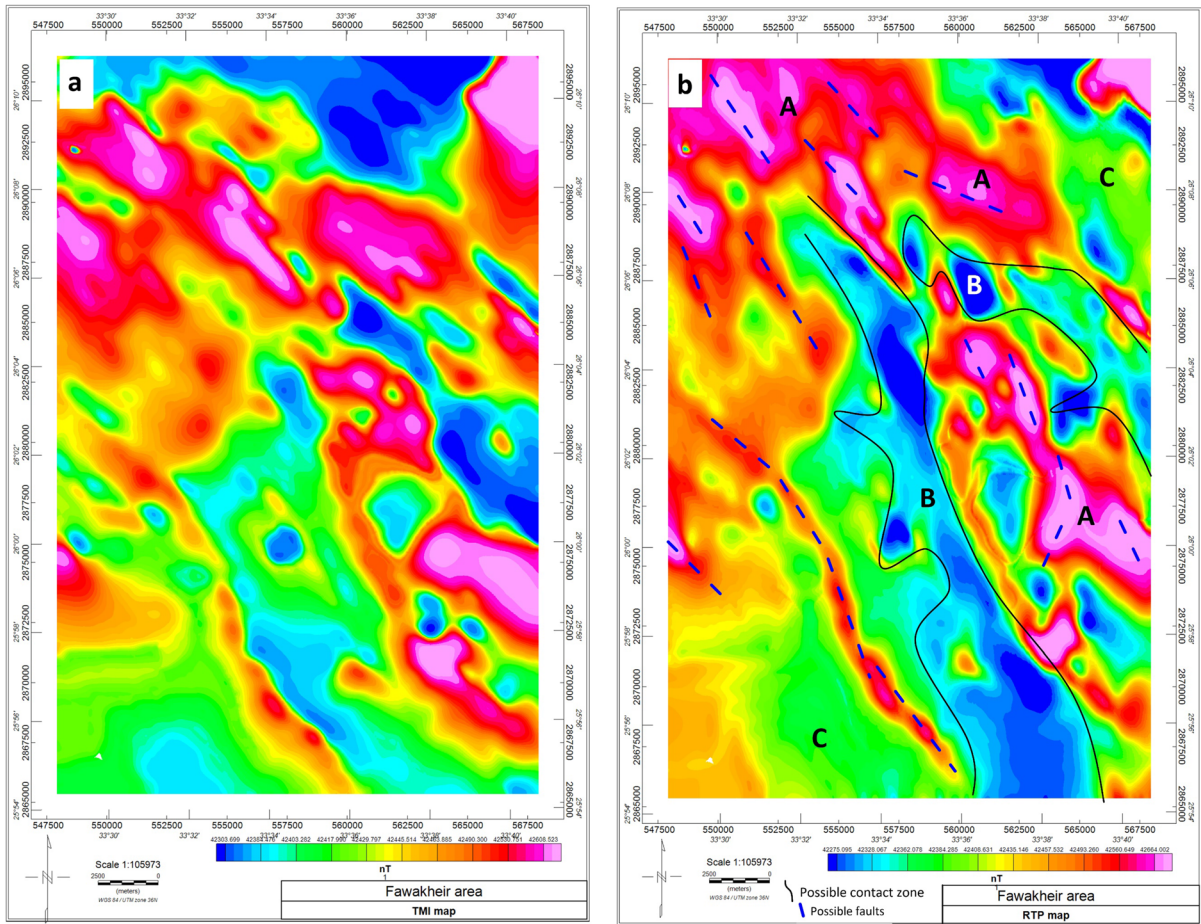


Figure 9

Total magnetic intensity map (a) and reduced to pole filtered map (b). Solid black lines surround zones of different magnetic textures, while dashed blue lines mark possible faults or fractures

the time of conducting the survey (1983) as  $d = 1.9^\circ$  and  $I = 32.8^\circ$ . The RTP map still shows the major magnetic zones shown on the total intensity map (Fig. 9a). Based on the magnetic relief, these zones can be categorised as follows:

**Blue zone:** This is a significant low-intensity magnetic zone ( $< 42,360$  nT) represented by anomalies B1 & 2. B1 anomaly corresponds to post-orogenic granite, while B2 is related to post-Hammamat felsite. This zone is cut by a system of thrust faults trending NW–SE. The green zone resembles a zone of intermediate magnetic intensity ( $\sim 42,360$  to  $42,457$  nT) marked by anomalies C1 and C2. The C1

anomaly overlays the Hammamat group while C2 represents metasediments and intermediate to acidic metavolcanic. The red and pink zone ( $> 42,457$  nT) is dominant over the entire study area and is characterised by a high magnetic intensity probably related to basement exposure rich in magnetite or rock units rich in magnetic minerals; this is marked as anomaly A1, A2, A3 and A4, where A1 corresponds to the NE metagabbro, A2 is due to south Attala metavolcanics, A3 resulted from the medium- to high-grade metamorphic rocks, and A4 is due to Hammamat group. The aforementioned rock units

and some gabbro to the south make up most of this high magnetic zone.

For interpreting magnetic maps, several transforms should be applied to enhance the desired signal and reduce ambiguity. Common transforms have some drawbacks, including reduction to pole (RTP), which is typically used as the initial step in deciphering magnetic data. It is necessary to know the inclination ( $I$ ) and declination ( $D$ ) of the source magnetisation and the present geomagnetic field when employing the RTP transform. The vector sum of induced and remanent magnetisations produces the observed magnetic field anomalies. A remanent magnetisation can be in any direction depending on its age and the subsequent rotations of the rock carrying it, whereas an induced magnetisation always has the same direction as the ambient geomagnetic field of the earth (except for extreme anisotropy or self-demagnetisation effects). However, when it is feasible to determine a source's effective remanent magnetisation, and because there is a lack of pertinent data regarding remanent magnetisation, remanent magnetisation is typically overlooked in magnetic field interpretation. Moreover, in this case, this uncertainty could make the RTP computation

unreliable and unstable (Silva, 1986), and the estimates of the source body characteristics that arise from incorrectly accounting for remanent magnetisation effects in an interpretation are inaccurate (including size, shape, dip and position).

To ensure the validity of the RTP filtered map for further processing, and to establish the general degree of the intrinsic content of remanence in the observed TMI data, we computed the Koenigsberger ratio ( $Q$ ). Its value is calculated for the general rock units in the area and is not indicative of a certain type. Hence, it can not be considered a solid indication of the remanence of the entire source bodies; however, we calculate it as a first indication of the magnetisation in the area. According to Helbig (1963), it determines the inherent content of remanence magnetisation in the data. It is feasible to determine the resulting magnetisation direction of a remanent magnetic substance remotely rather than by building a model. The resulting magnetisation offers a first-order indicator of remanence content as we mentioned. When calculating  $Q$  using Helbig (1963), it is found around 1.1545648, i.e.,  $Q$  is close to 1, according to the findings; hence, the remanence content is

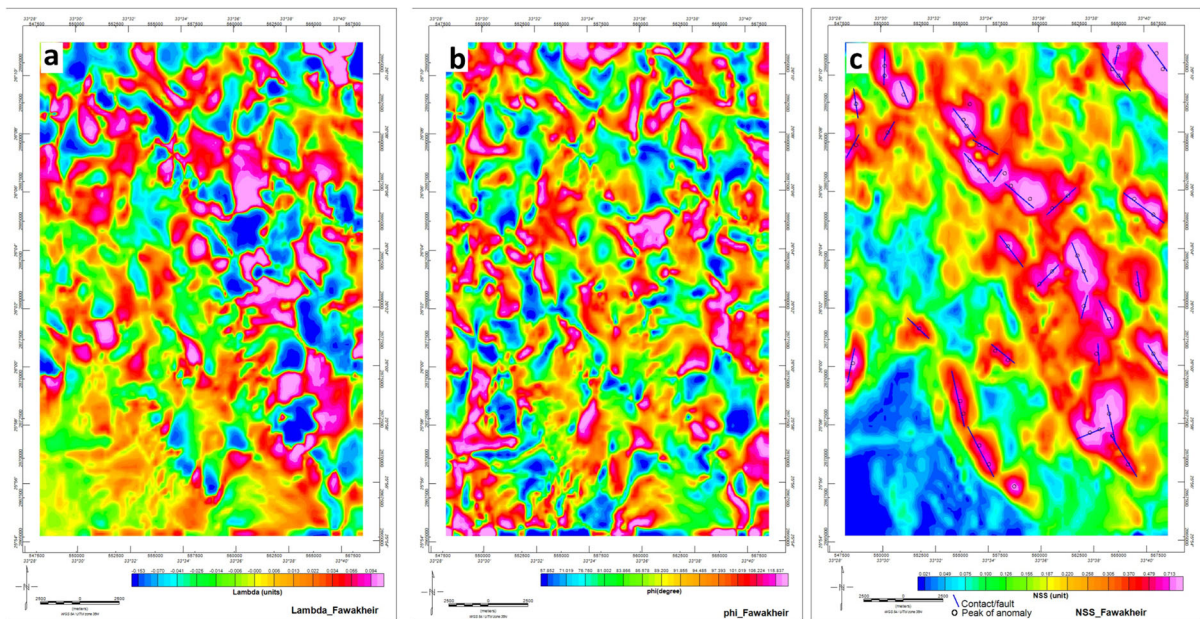


Figure 10  
Normalised source transformation. The intermediate eigenvalue  $\lambda_2$ (a), angle  $\phi$  (b), and  $\mu$  map (c)

acceptable and the RTP may still be utilised for additional magnetic inversion.

To ensure the validity of the magnetic data used, the normalised source strength transformed anomaly map (NSS) or  $\mu$  map, the intermediate eigenvalue  $\lambda_2$  and the angle  $\varphi$  are calculated. The magnetic gradient tensor is the basic component of the NSS. The benefit of using NSS is that it is not affected by the magnetisation direction of the source and only slightly by the local magnetic field. Moreover, magnetic sources and their depths may be simply determined since they fulfil the Euler equation. For detailed mathematical derivations, the author refers to Beiki et al. (2012). When geological sources possess remanent magnetism, the analytic signal filter (AS) can offer less trustworthy information regarding the source geometry compared to the NSS (Beiki et al., 2012). For the Fawakheir region, the normalised source strength transformation map  $\mu$ , together with the two complimentary maps,  $\varphi$  and  $\lambda_2$  are calculated (Fig. 10a,b,& c).

Edge detection filters are very common in magnetic interpretation. Their aim is the possible tracking of the magnetic lineations, contacts, rock unit boundaries and faults. It is a very effective technique in exploring mineralisation zones, where it is commonly associated with the suture or fracture zones. Among these filters are the analytic signal (AS), Euler deconvolution (ED), tilt angle (TA) and magnitude magnetic transforms (MMTS). In the AS filter, the analytical signal or total gradient (a) is produced by combining the diagonal portions of the horizontal and vertical magnetic tensor. The horizontal coordinate and depth of the causative body, rather than the magnetisation direction, determine the form of the analytical signal across that body.

The tilt filter is described in Gobashy et al., 2021b; Miller & Singh, 1994; Salem et al., 2007; Verduzco et al., 2004. In this filter, the local amplitude of the field gradients determines how much of an amplifier this filter is, and the filter output does not retain any amplitude information. The Euler deconvolution filter is a semi-automatic approach that was performed on the RTP map to quantitatively quantify the depth of the causal source of the magnetic anomalies and the possible lineation of the magnetic signals. Euler's homogeneity equation

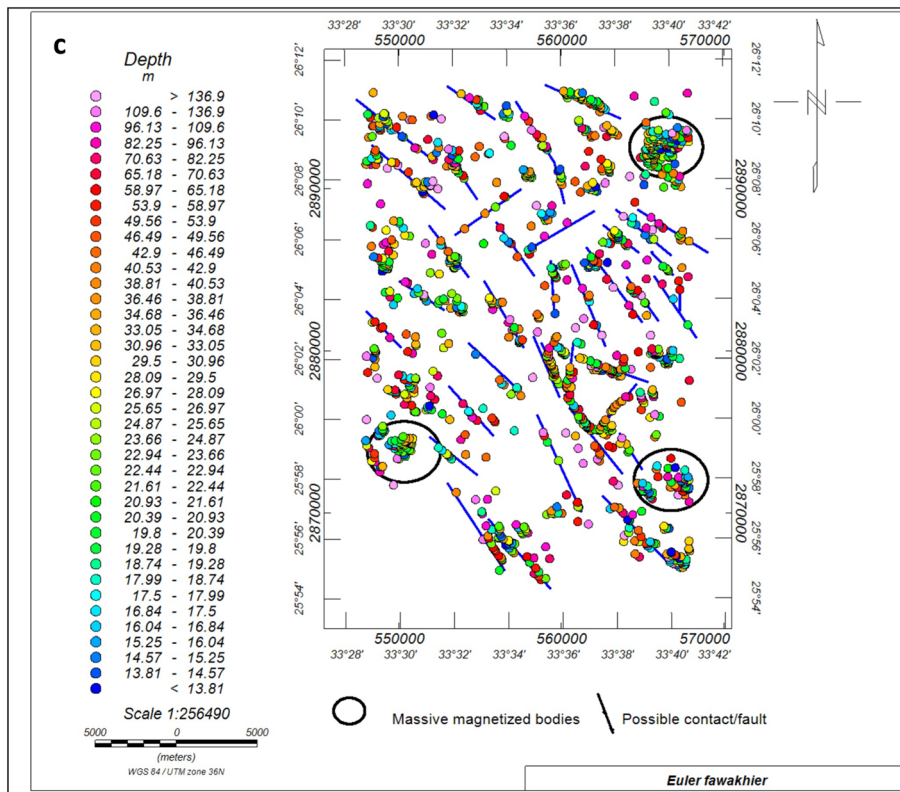
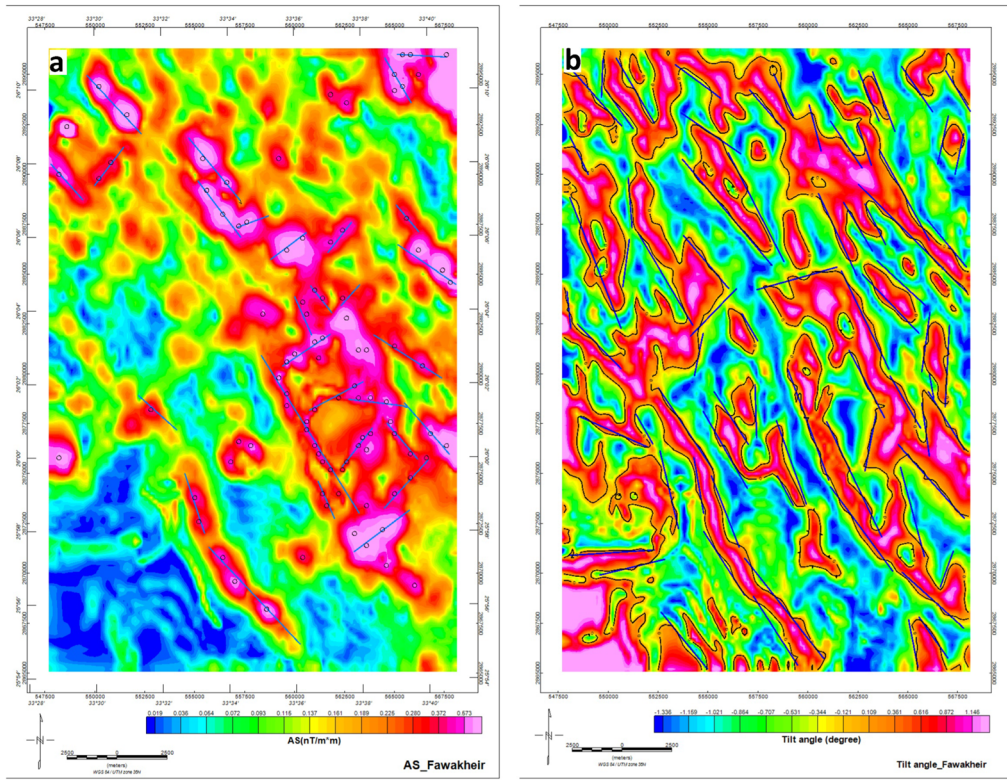
in three dimensions (3D) (Reid et al., 1990; Thompson 1982). Figure 11 shows the AS, ED and TA filters. Results conform to the general NW–SE dominant trends and association of different rock units to the observed trends. In Fig. 11a, the analytic signal anomalies are dominated by the NW–SE trend. Further geological interpretation is given in the next sections.

The magnitude magnetic transform (MMTS) enhances the signal over the noise in the measured magnetic data and overcomes knowledge of the inclination and declination of the source magnetisation vector of the magnetised body as well as that of the ambient geomagnetic field. The MMTS presented by Stavrev and Gerovska (2000) is based on the total magnitude anomaly (TMA) and is called magnitude magnetic transform (MMTS). They include the TMA itself (Ta), modulus of the full gradient of the TMA (R), Laplacian of TMA (L), half of the square root of the Laplacian of the square of the TMA (E) and square root of the product of the TMA and the Laplacian of the TMA (Q). These transforms exhibit a significantly higher degree of centricity to causative sources than the measured anomalous field Stavrev & Gerovska, 2000; Gerovska et al., 2004; Stavrev, 2006. They also have non-negative distributions, anomaly patterns that are less sensitive to the direction of the magnetisation vector than the TMA itself and non-negative distributions. The results of the above filtering are shown in Fig. 12. Faults and contacts are posted as solid lines to the different transforms.

Finally, the CET (Centre for Exploration Targeting) grid analysis technique is applied to examine an image's texture to identify areas of structural complexity and, as a result, assess the likelihood of the existence of a gold deposit. This method first locates magnetic discontinuities, then identifies areas of discontinuity and analyses structural linkages to detect crossings, junctions or contacts, and changes in direction in the strike. It makes it easier to select the locations that are promising (Holden et al., 2008). Consequently, the method entails the following steps: texture analysis, texture ridge detection and thinning of texture ridges.

Several useful maps have resulted from such analysis including standard deviation (STD),





◀Figure 11  
Edge detection filters. The analytic signal (a), tilt angle (b) and the Euler deconvolution (c). Circles in (c) indicate massive source bodies

orientation entropy (OE) and contact occurrence map (COD) or heat map. The STD displays the range of greyscale pixel intensities, while the OE map focuses on locations where structures can be found in a variety of orientations, hence highlighting possible

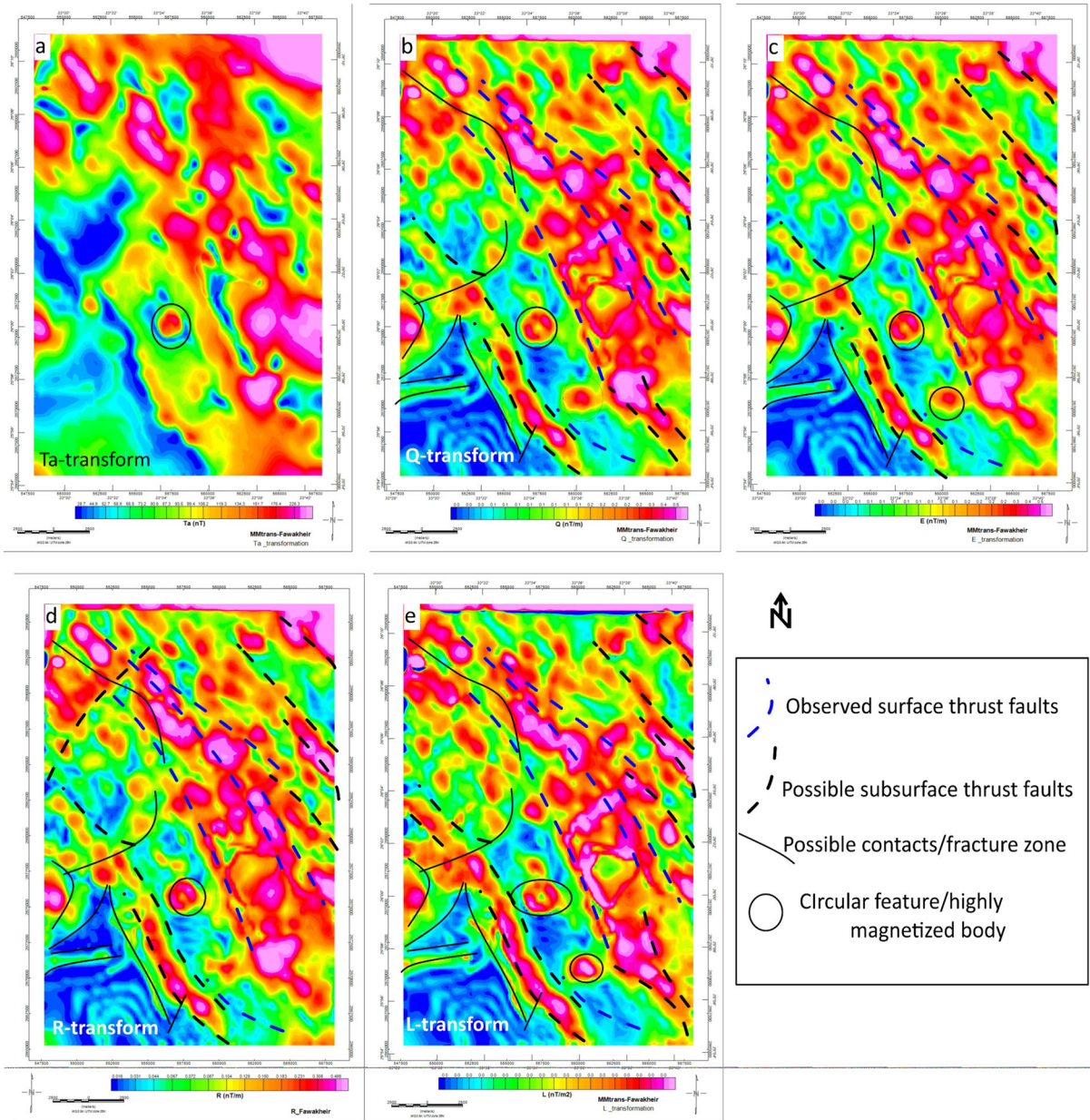


Figure 12  
Magnitude magnetic transform maps (MMTS) with preliminary interpretation. Ta (a), Q (b), E (c), R (d) and L (e)

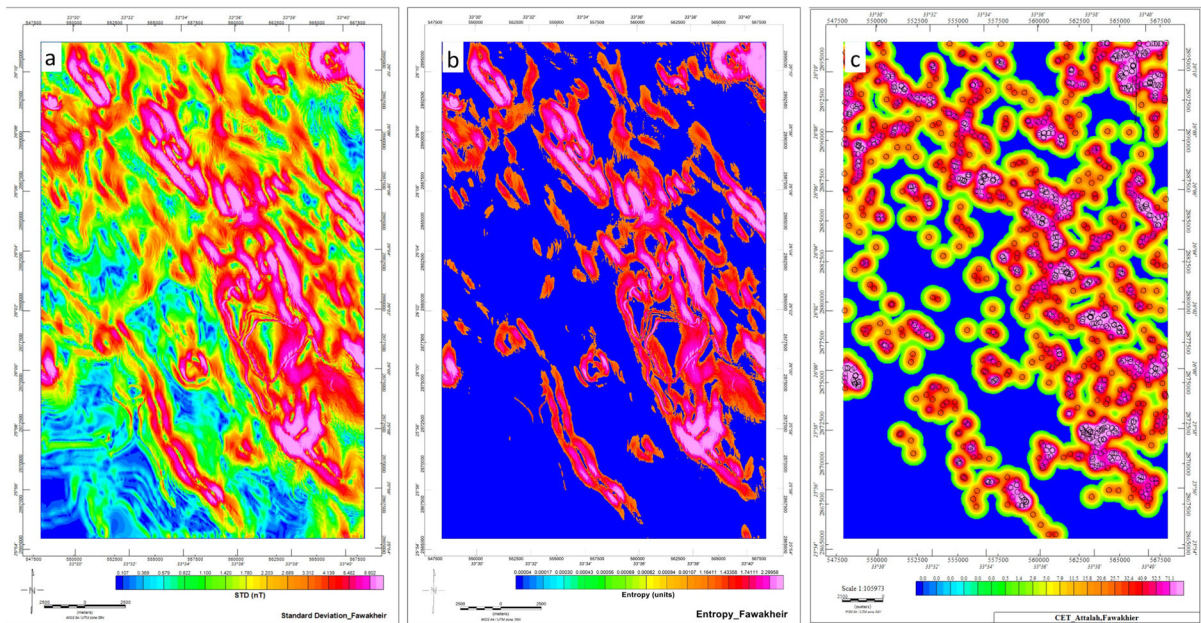


Figure 13

CET grid analysis. Standard deviation (a), orientation entropy (b) and contact occurrence density (c) with the probable location of expected Au mineralisation zones

structural complexity. The COD gives a direct indication of the zones of complex structures which represent probable location mineralisation.

Results of such grid analysis are represented in Fig. 13. Based on the orientation entropy structural complexity pattern and STD map, (Fig. 13a, b), the COD (heat) map (Fig. 13c) is presented that addresses the probable locations of Au mineralisation associated with strong shearing and fracture zones. This is identified by circles distributed all over the study area.

## 5. Results and Interpretation of Aeromagnetic Data

### 5.1. Faults

Possible faults are interpreted mainly from the NSS and tilt data (Fig. 14 a,b). Both the interpreted faults and faults determined from the geological mapping are posted on their corresponding maps for comparison (Fig. 14a, b). Many of the geologically mapped faults are clear in the aeromagnetic data.

Most faults are of NW to NNW trends, and less frequently have N-S to NNE and E-W directions. Faults interpreted from the aeromagnetic data that are not recorded on the surface geological mapping probably represent subsurface structures or rock contacts. The faults resulting from geological mapping and faults interpreted from NSS data are projected on the orientation entropy (OE) map and presented in Fig. 14c. The entropy values indicate strong fracturing and faulting along the NW trend. The projected faults remarkably delineate and run along with the high entropy values.

### 5.2. Rock Units

The geological map is projected on the NSS, and  $\lambda_2$  maps show the magnetic signature of the different rock units (Fig. 15a, b). Three gold mines are present in the study area. Atalla mine is at the extreme NW part of the mapped area. Fawakheir mine is in the south-central part. El Sid mine is at the SW part. The locations of these mines are represented by white circles on the maps. Careful inspection of the

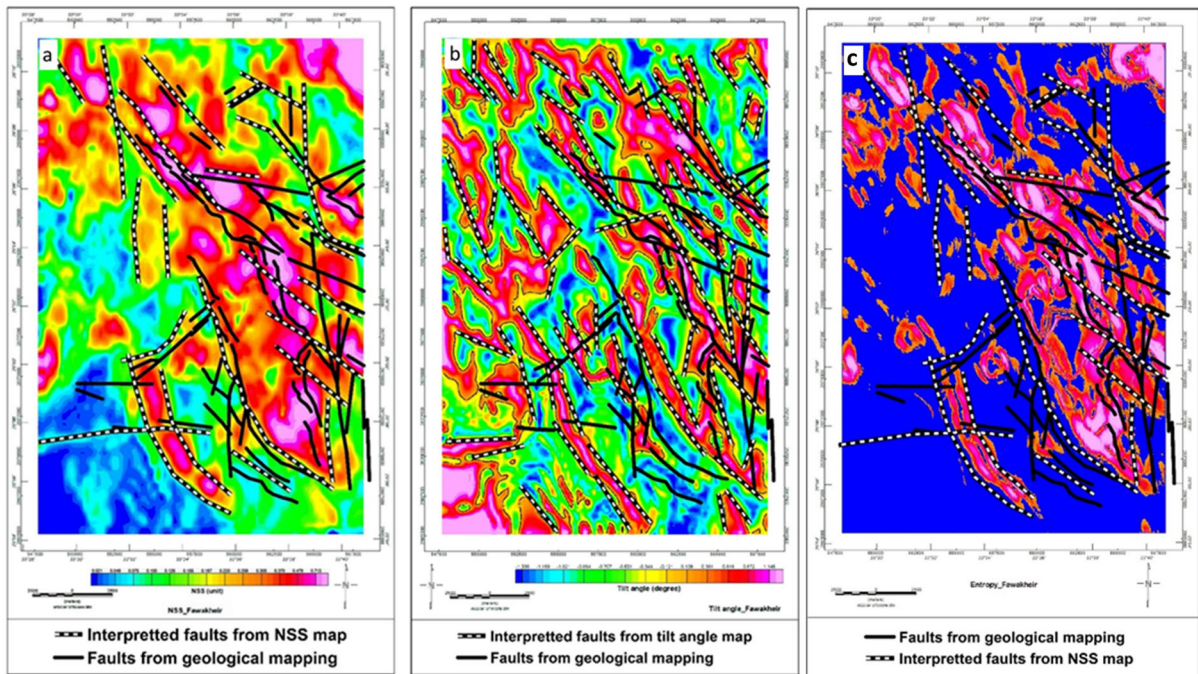


Figure 14

**a** Faults from geological mapping and faults interpreted from NSS data posted on NSS map, **b** faults interpreted from tilt data posted on the Tilt map. **c** Faults from geological mapping and faults interpreted from NSS data posted on the entropy map. The blue and red colours represent minimum and maximum entropy values, respectively

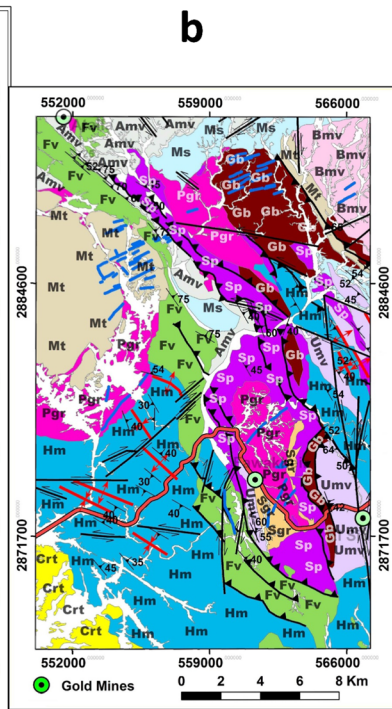
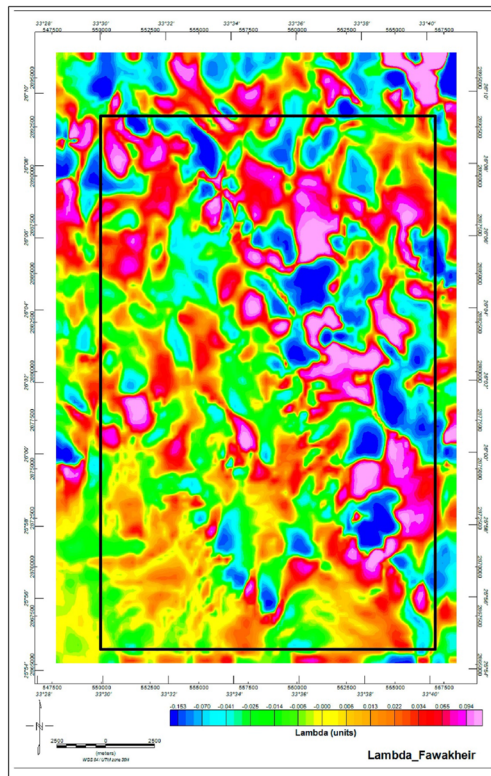
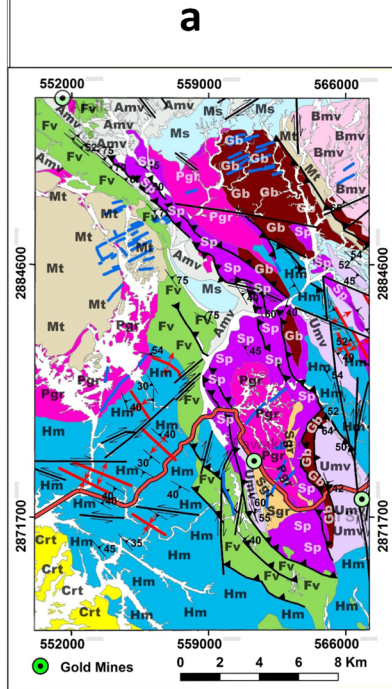
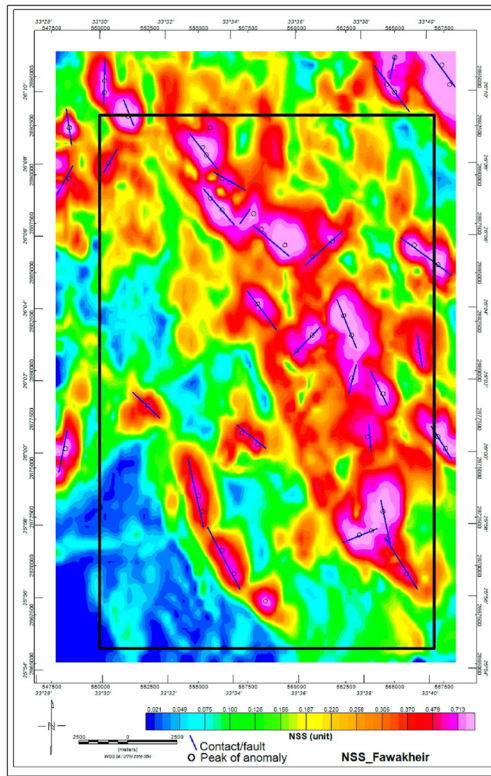
integrated geology and filtered magnetic maps shows a variable magnetic signature of the different rock units. The variation in the magnetic anomaly within the same rock unit in the same magnetic data type is probably due to mineralogical composition variations within this unit. Table 3 summarises the results of this analysis.

### 5.3. Euler Depth Maps

The faults and contacts interpreted from the Euler convolution data together with the depth points and point cluster solutions are projected on the tilt angle map (Fig. 16). The determined point cluster solutions are projected on the geological map. Figure 17 shows the geological interpretation of these clusters. These figures show that a considerable number of the Euler solution depths coincide with the zero contours of the tilt angle map, which indicates that these Euler points are associated with subsurface contacts or faults. The three gold mines in the area lie on or close to the zero

contour of the tilt angle map, which indicates that this gold occurrence is associated with subsurface faulting and shearing. The northeastern clustered solution (Fig. 17) lies along the lithological contact between the metasediments and the basic metavolcanics. The southeastern clustered solution lies in the undifferentiated metavolcanics and no surface lithological contact is observed at this location. It probably represents a subsurface contact between the undifferentiated metavolcanics and metagabbro, since the metagabbro mass is located to the west of the undifferentiated metavolcanics and the contact dips eastward. The southwestern clustered solution lies in the Hammamat group. It probably represents a subsurface contact between the Hammamat sediments and the post-orogenic granite that lies to the north of the cluster, since this contact dips southwards.

Alongside the aeromagnetic data available, a detailed land magnetic survey was conducted along selected profiles crossing the rock units of interest for



◀Figure 15

**a** The geology of the study area correlated with the NSS map. *Crt* Cretaceous sediments, *Fv* post-Hammamat felsite, *Hm* Hammamat group, *Pgr* post-tectonic granite, *Sgr* syn-tectonic granite, *Amv* intermediate to acidic metavolcanics, *Umv* undifferentiated metavolcanics, *Bmv* basic metavolcanics, *Ms* metasediments, *Mg* metagabbro, *Sp* serpentinite, *Mt* medium- to high-grade metamorphic rocks. White circles are gold mines. Atalla mine is at the extreme NW part of the mapped area. Fawakheir mine is in the south-central part. El Sid mine is at the SW part. **b** The geology of the study area correlated with the  $\lambda_2$  map

further magnetic tomographic inversion. The data were gathered using Geometrix G-857 proton precession magnetometer; station spacing ranges between 20 and 50 m. The data were then corrected for diurnal variation using base station magnetometer data. Then, a simple Gaussian filter was applied to remove cultural noise. A total of 94 stations were collected along 13 profiles as shown in Fig. 18. The tomographic inversion is performed assuming the two-dimensional earth model consists of a large number of prismatic cells each with an unknown magnetic susceptibility value. A hybrid combination includes the Marquardt algorithm (Marquardt, 1963) and focused regularisation technique (Portniaguine &

Zhdanov, 1999). The Zondgm2d software is used for such a process. The resulting tomographic section represents a possible distribution of the subsurface magnetic susceptibilities along the selected profiles. All modelled profiles are projected to central straight profiles that best fit each profile separately. This process is necessary for preparing the data for inversion along a regular array of data. Each profile has its colour scale because of the large difference in magnetic susceptibility magnitudes that prevent unifying the scale. However, low susceptibility values are shown with blue colours and high values with red and pink colours. Surface magnetic susceptibilities are also measured using a K-20 magnetic susceptibility meter along all profiles. The observed measurements are used as a priori information to constrain the inverted profiles.

### 6. Geological Interpretation of Land Magnetic Profiles

The geological interpretation of the magnetic profiles is based on the data available from the detailed geological mapping and structural studies

Table 3

*Signatures of the different rock units on the normalised sources' strength and intermediate eigenvalue maps*

Rock unit	Magnetic signature and data type	
	NSS or $\mu$ map	$\lambda_2$ map
Atalla gold mine	High	Low
Fawakheir gold mine	High	Intermediate
El Sid gold mine	Intermediate	high
Medium to high-grade metamorphic rocks	Low to intermediate	Intermediate to high
Serpentinite	High to very high	Low to intermediate
Metagabbro	High	High to very high
Metasediments	Intermediate to high	Low to intermediate
Basic metavolcanics and the undifferentiated metavolcanics	Variable anomalies (from low to high anomalies)	Intermediate to very high
Intermediate to acidic metavolcanics	Intermediate to high	Low to high
Syn-orogenic granite	High to a very high	Low to intermediate
Post-orogenic granite	Intermediate to very high	Intermediate to very high
Hammamat Group	Low anomaly, except along an NW trending linear zone of very high	Intermediate to high
Post-Hammamat felsites	Intermediate to high	Intermediate to high
Cretaceous sediments	Low	Intermediate

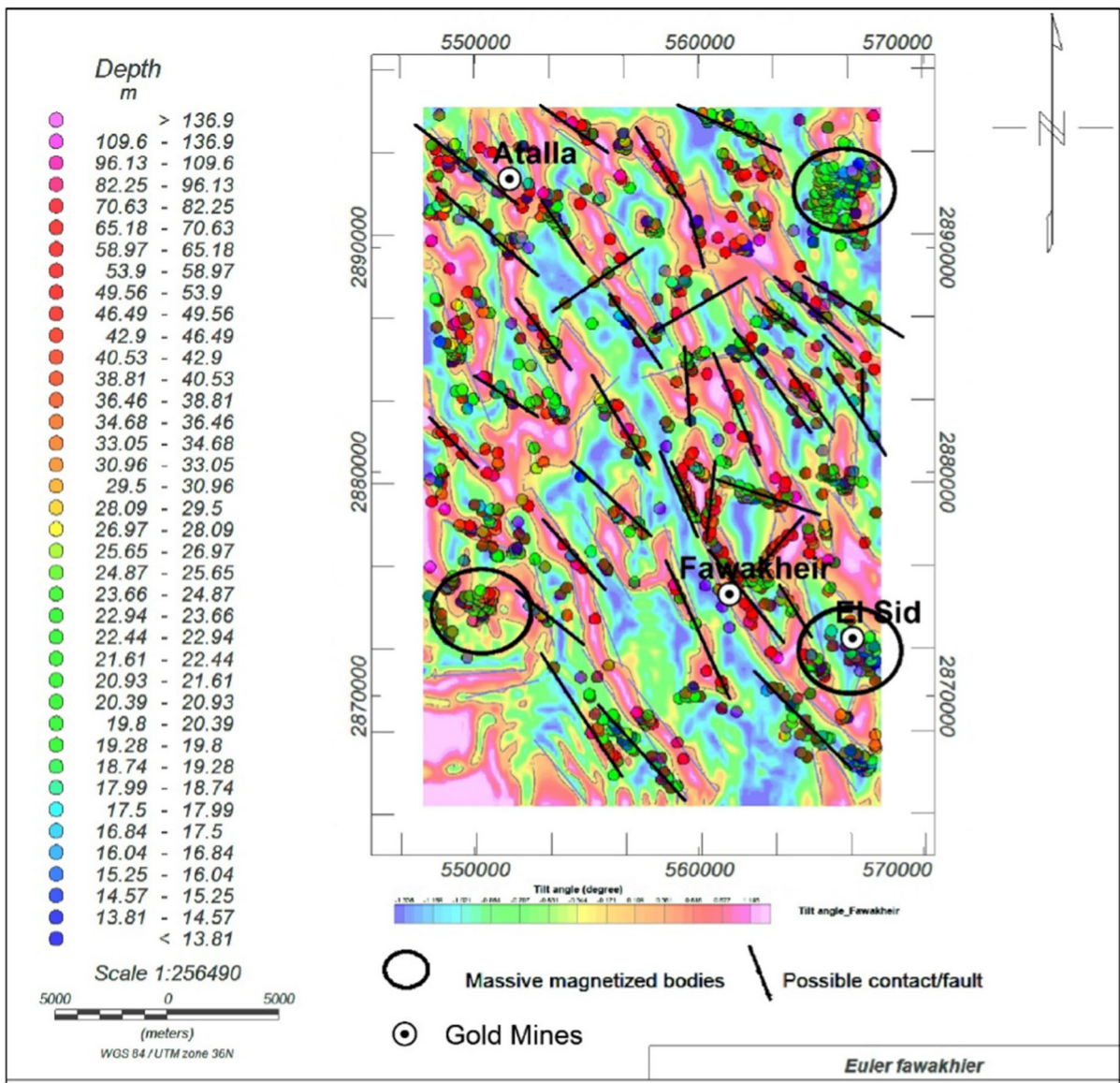


Figure 16

The Euler convolution depth points, point cluster solutions and interpreted faults and contacts posted on the tilt angle map in which the zero-contour is illustrated. White circles are locations of gold mines. Atalla mine is in the extreme NW part of the mapped area. Fawakheir mine is in the south-central part. El Sid mine is in the SW part

were done on the area. Only the interpretation of profiles 5, 6 and 7 are presented.

6.1. Profile P5

The profile runs in three sectors trending SW-NE, NW-SE and SW-NE from the start of the traverse,

with a total length of about 24 km (Fig. 18). The traverse runs at its middle part close to El-Fawakheir gold mine. The closest point to the mine is marked on the magnetic profile (Fig. 18). Geologically, Fig. 19a shows a serpentinite mass at the start of the profile capped by Hammamat sediments and post-Hammamat felsites along stratigraphic contacts. The

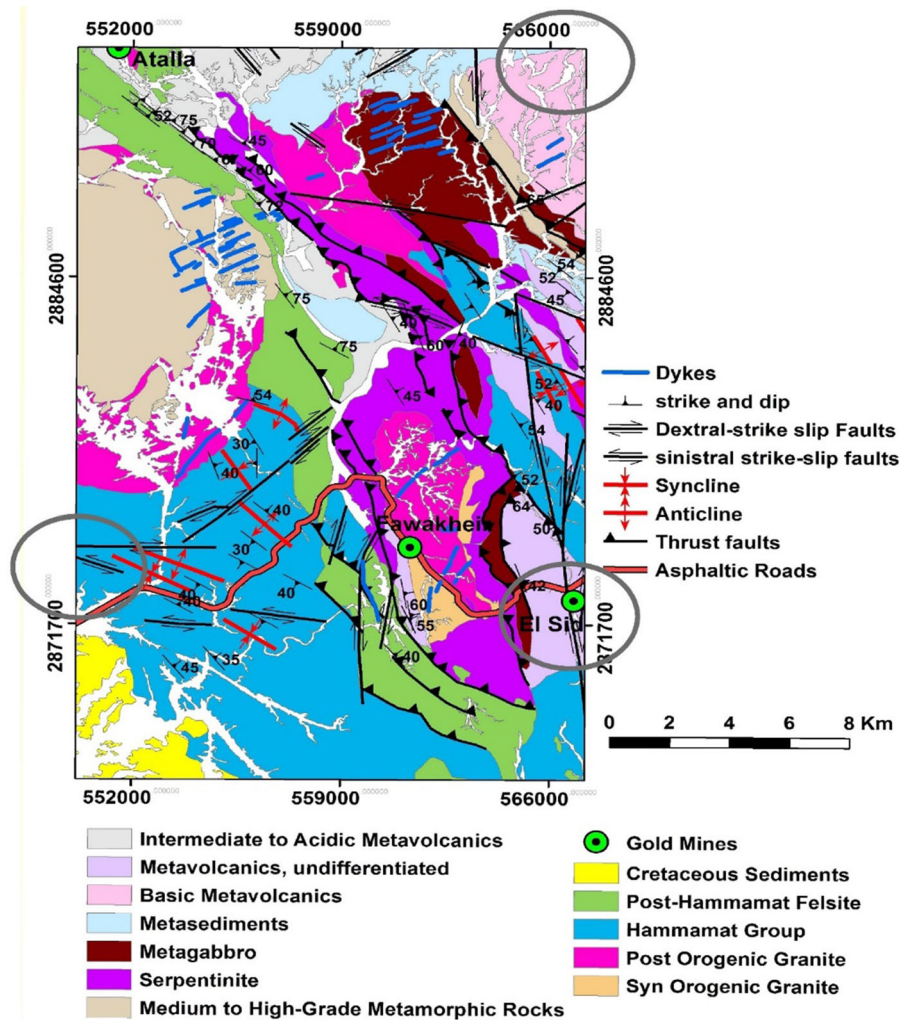


Figure 17

Locations of detected Euler's massive magnetised bodies (large green circles) projected on the geological map. Light green small circles are locations of gold mines. Atalla mine is at the extreme NW part of the mapped area. Fawakheir mine is in the south-central part. El Sid mine is at the SW part

serpentinite is associated with a high magnetic anomaly, while the latter two units are associated with a low anomaly. At the central part of the traverse, the serpentinite is intruded by the post-orogenic granite and over-thrusted by the basic metavolcanics and metagabbro; it is in contact against the basic metavolcanics along a strike-slip fault. The metagabbro is associated with medium anomaly and the basic metavolcanics reflect low magnetic anomaly. Outside the eastern margin of the mapped area, the basic metavolcanics are in structural contact against the Hammamat sediments along a

strike-slip fault and also occur in the subsurface of the profile. The gold occurrence is within the basic metavolcanics associated with the low magnetic anomaly.

## 6.2. Profile P6

The profile extends for about 6 km along the SSW-NNE trend. It runs totally in serpentinite (Fig. 19b), which shows medium to low magnetic anomaly due to the considerable alteration to talc-carbonate rocks as indicated in the field. It is affected



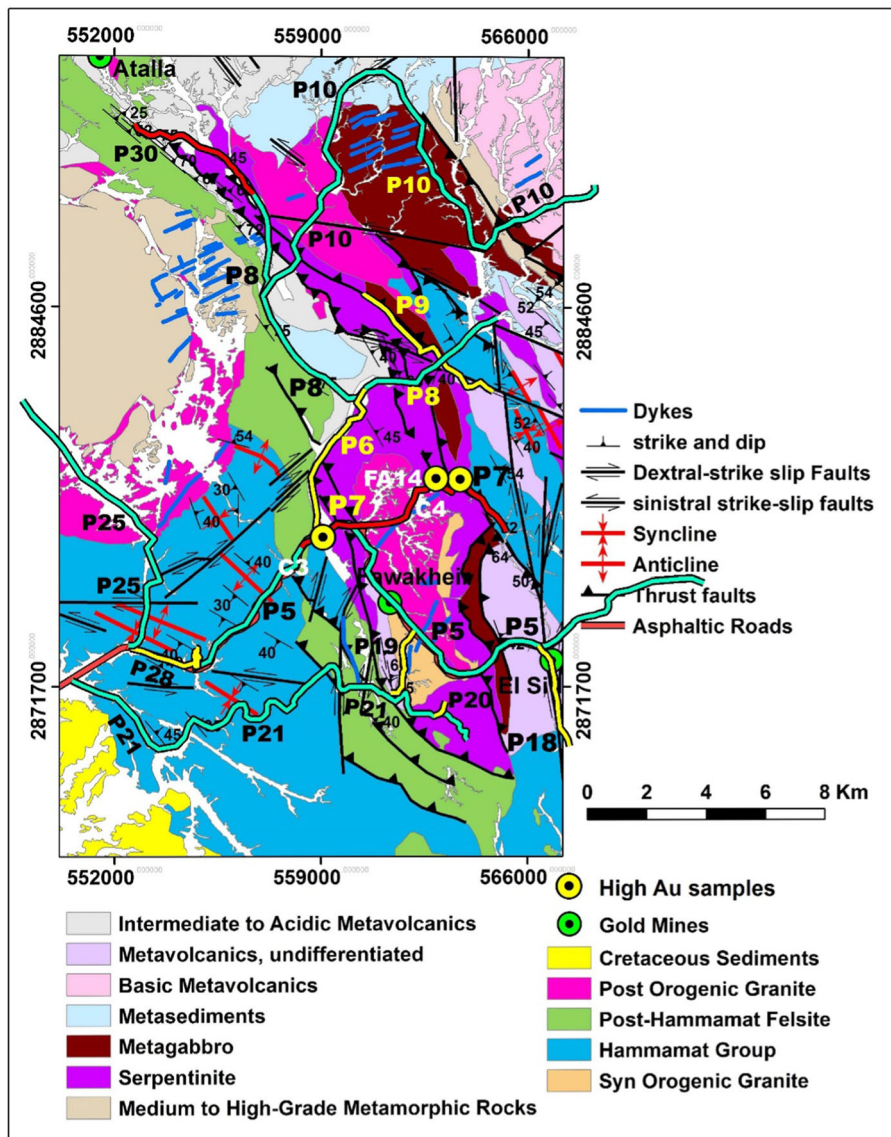


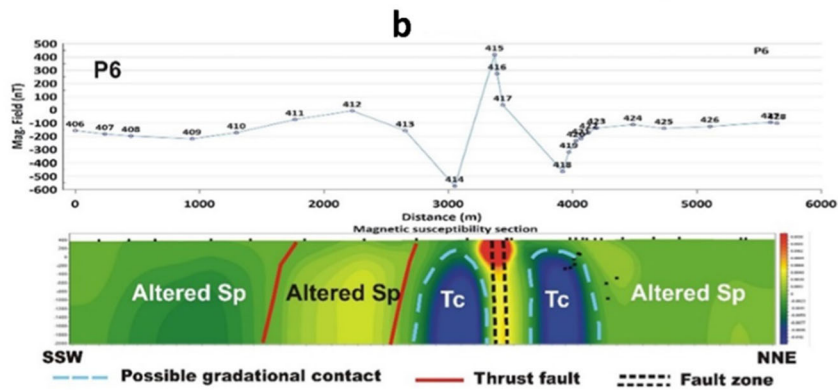
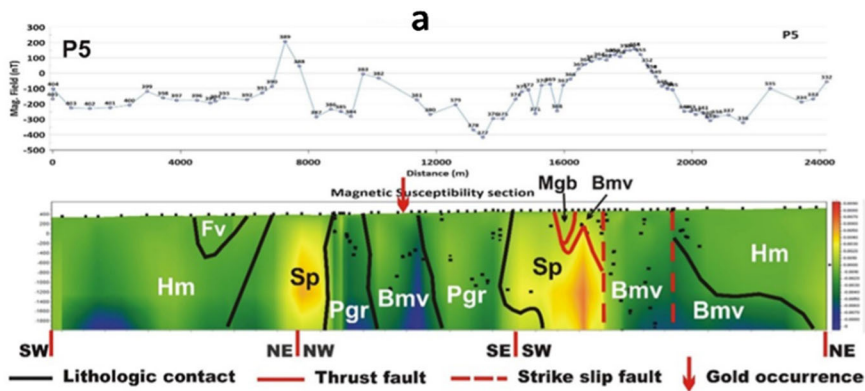
Figure 18

Geological map of Fawakheir area showing the distribution of the surveyed magnetic profiles and locations of high Au samples

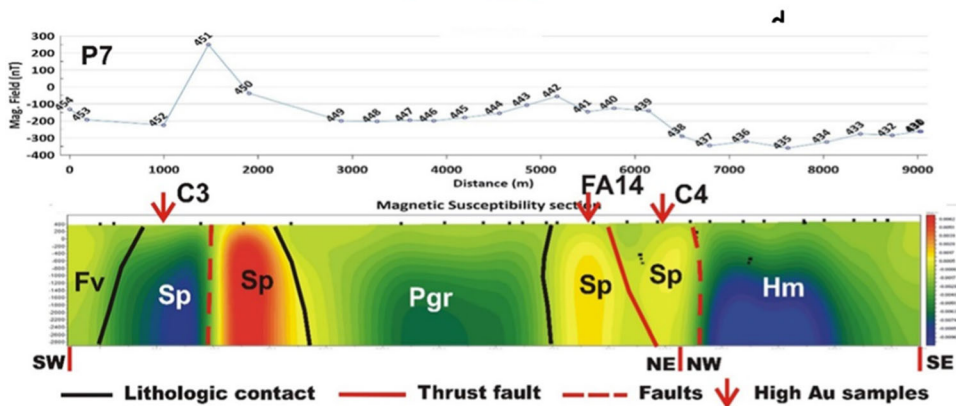
by two parallel thrusts and a fault zone that shows a high magnetic anomaly pointing to the possible concentration of iron oxides. The satellite image of this fault zone indicates three minor strike-slip faults affecting this part of the traverse (Fig. 19c). The two low anomaly zones surrounding the fault zone are probably talc carbonates.

### 6.3. Profile P7

The traverse runs for about 9 km along two sectors of SW-NE and NW-SE trends (Fig. 18). It cuts across the post-orogenic granite (El Fawakheir granite) at its northern parts. The post-orogenic granite is intrusive in the serpentinite rocks (Fig. 19d). The latter is in structural contact against the post-Hammamat felsites and the Hammamat sediments along two strike-slip faults at the start



**C**



◀Figure 19

**a** Geological interpretation of the magnetic field of profile P5. **b** Geological interpretation of the magnetic field of profile P6. **c** High-resolution satellite image showing a fault zone consisting of three minor strike-slip faults cutting across profile 6. Yellow circles are traverse stations. Note the remarkable alteration of the serpentinite to talc carbonates. **d** Geological interpretation of the magnetic field of profile P7 with the posted locations of Au samples. *Sp* serpentinite, *Mgb* metagabbro, *Bmv* basic metavolcanics, *Pgr* post-orogenic granite, *Hm* Hammamat group, *Fv* post-Hammamat felsites, *Tc* talc carbonate

and end of the profile, respectively. The serpentinite mass in the central part of the profile is affected by a thrust fault of NNE-SSW trend. The serpentinite shows low to high magnetic anomaly due to alteration, while the post-orogenic granite, Hammamat group and post-Hammamat felsites are of low anomaly. Three samples of high Au content lie along this profile (C3 = 1.5 ppm Au; FA14 = 9.5 ppm Au; C4 = 5 ppm Au). All of these samples are located within the altered serpentinite rocks of low to intermediate magnetic anomaly.

### 7. Conclusions

The following findings are made based on an integrated investigation and comparison of the outcomes from several methodologies, including geological site investigation, remote sensing and various magnetic filters.

1. Compatibility between the magnetic data in the different profiles and the mapped rock units and the structural framework of the Fawakheir area is observed. The contacts between the different rock units and fault planes are easily traceable on the magnetic profiles. The high magnetic anomalies and magnetic susceptibilities in the Fawakheir area, in general, are related to the magnetite content in the serpentinite as evidenced by the geochemical analysis.
2. The syn-orogenic rock units (serpentinite, talc carbonate, metagabbro, metasediments, basic metavolcanics, intermediate to acidic metavolcanics) are in either lithological or structural contact against each other. Structural contacts are along thrusts or strike-slip faults.
3. The talc-carbonate rocks are in gradational contact with the serpentinite. The syn-orogenic rock units are intruded by the syn- and post-orogenic granites and capped by the Hammamat group and post-Hammamat felsites; the contact is stratigraphic in most cases. Masses of the post-orogenic granite are possibly present in the subsurface of some profiles. In some traverses, the Hammamat group and post-Hammamat felsites are very thick and extend to the bottom of the profile.
4. The exposed fault planes can be traced in the magnetic profiles. Some strike-slip faults show a remarkable increase of the magnetic field along their planes due to intensive shearing and probable concentration of iron oxides by hydrothermal solutions.
5. The talc-carbonate rocks are associated with a low magnetic anomaly. This is a remarkable magnetic signature. They are in gradational contact against the serpentinite. The latter has medium to high magnetic anomaly except when partially altered to talc carbonate where it attains low to medium anomaly.
6. The syn-orogenic granite is associated with higher magnetic anomalies than the post-orogenic granite. The latter shows different signatures of its magnetic anomaly from one location to another that may point to the inhomogeneity of its composition.
7. The metagabbro shows medium to high anomaly except in one location (in P10) where it attains low anomaly because of the presence of numerous injections by the post-orogenic granite.
8. The basic metavolcanics and intermediate to acidic metavolcanics reflect variable magnetic anomalies that may point to the inhomogeneity of their composition.
9. The post-Hammamat felsites and Hammamat group show low magnetic anomaly, except in profile P 25, where a very high anomaly is recorded in the latter because of the presence of a strike-slip fault and in profile P8 because of a possible concentration of iron oxides in this part of the unit.

10. The relation between the contacts or fractures and the comparison with the COD-filtered magnetic map suggest new criteria for possible locations for AU occurrences (Fig. 13c).
11. The serpentinite sample FA14 contains exceptionally high gold content (9.5 ppm). This sample also shows the highest Ni content (3126 ppm) and MgO/SiO<sub>2</sub> ratio (0.94) compared to the analysed rocks from the Golden Triangle. The corresponding magnetic anomaly is associated with faults/contacts/and or thrust faults. This is evident from the contact occurrence density map and the 2D tomographic inversion (Fig. 18d).
12. Two of the serpentinite samples contain 0.3 and 0.5 ppm gold, which are lower than the carbonatized samples (1.6 and 5 ppm).
13. The suggested approach for locating Au mineralisation zones using integrated COD, NSS, tilt magnetic maps and magnetic tomographic modelling, along with RS and geochemical data, may be applied to other regions with comparable complex structures for Au mineralizations.

### Acknowledgements

Abdelmonem EL-DougDoug wishes to acknowledge the Science, Technology and Innovation Funding Authority (STDF) for making this research possible and funding project no. 26277, “Exploring carbonatized ultramafic rocks (listvenite) for gold occurrences in the Qena-Safaga-Quseir area (Golden Triangle) and its impact on development plans, Eastern Desert, Egypt”; the Faculty of Science at Cairo University and the Geology Department’s assistance with logistics and permissions, as well as the preparation of thin sections and sample coring.

**Author Contributions** AED contributed to the conceptualization of the research; MG and MA conducted, processed and interpreted geophysical data; MAE-W contributed to structural work and the supervised remote sensing section provided by AA; YAE-R conducted the petrophysical study; Said Said contributed to the geology and field site geological work together with the other team members. All authors have read and agreed to the published version of the manuscript.

### Funding

Open access funding provided by The Science, Technology & Innovation Funding Authority (STDF) in cooperation with The Egyptian Knowledge Bank (EKB). Open access funding is provided by The Science, Technology & Innovation Funding Authority (STDF) in cooperation with the Egyptian Knowledge Bank (EKB).

### Data Availability

The data that support the findings of this study are available from the corresponding author upon reasonable request.

### Declarations

**Conflict of Interest** The authors declare no conflict of interest.

**Open Access** This article is licensed under a Creative Commons Attribution 4.0 International License, which permits use, sharing, adaptation, distribution and reproduction in any medium or format, as long as you give appropriate credit to the original author(s) and the source, provide a link to the Creative Commons licence, and indicate if changes were made. The images or other third party material in this article are included in the article’s Creative Commons licence, unless indicated otherwise in a credit line to the material. If material is not included in the article’s Creative Commons licence and your intended use is not permitted by statutory regulation or exceeds the permitted use, you will need to obtain permission directly from the copyright holder. To view a copy of this licence, visit <http://creativecommons.org/licenses/by/4.0/>.

**Publisher’s Note** Springer Nature remains neutral with regard to jurisdictional claims in published maps and institutional affiliations.

### REFERENCES

- Abd El Monsef, M. (2020). Ore controls and metallogenesis of au-ag deposits at Atalla mine, central eastern desert of Egypt. *Acta Geologica Sinica*, 94, 1451–1470.
- Abd El-Rahman, Y., Polat, A., Dilek, Y., Kusky, T. M., El-Sharkawi, M., & Said, A. (2012). Cryogenian ophiolite tectonics and metallogeny of the central eastern desert of Egypt. *Ore Geology Reviews*, 54, 1870–1884.
- Abd El-Wahed, M. A. (2009). The role of the Najd Fault System in the tectonic evolution of the Hammamat molasse sediments,

- Eastern Desert, Egypt. *Arabian Journal of Geosciences*, 3(1), 1–26. <https://doi.org/10.1007/s12517-008-0030-0>
- Abdeen, M. M., Thurmond, A. K., Abdelsalam, M. G., & Stern, R. J. (2001). Application of ASTER band-ratio images for geological mapping in arid regions: the Neoproterozoic Allaqi Suture Egypt. In: Proceedings of GSA 2001 Annual Meeting, Boston.
- Abdelazeem, M., El-Sawy, E. S. K., & Gobashy, M. M. (2013). Analysis of magnetic gradients at North East of Wadi Ar Rika quadrangle, Saudi Arabia, to delineate subsurface linear features and faults. *NRIAG Journal of Astronomy and Geophysics*, 2(1), 27–38.
- Abdelazeem, M., Fathy, M. S., & Gobashy, M. (2021). Magnetometric identification of sub-basins for hydrocarbon potentialities in Qattara Ridge, North Western Desert Egypt. *Pure and Applied Geophysics*, 178(3), 995–1020.
- Abdelazeem, M., & Gobashy, M. M. (2016). A solution to unexploded ordnance detection problem from its magnetic anomaly using Kaczmarz regularization. *Interpretation-A Journal of Subsurface Characterization*, 4(3), S61–S696. <https://doi.org/10.1190/INT-2016-0001.1>
- Abdelazeem, M., Gobashy, M., Khalil, M. H., & Abdrabou, M. (2019). A complete model parameter optimization from self-potential data using Whale algorithm. *Journal of Applied Geophysics*, 170, 103825.
- Abdelazeem, M., Mekkawi, M., & Gobashy, M. (2014). Subsurface structures using a new integrated geophysical analysis, South Aswan Egypt. *Arabian Journal of Geosciences*, 7(12), 5141–5157. <https://doi.org/10.1007/s12517-013-1140-x>
- Abdelhalim, A., Aboelkhair, H., Hamimi, Z., & Al-Gabali, M. (2020). Mapping lineament features using GIS approaches: case study of neoproterozoic basement rocks in the south-eastern desert of Egypt. *Arabian Journal of Geosciences*, 13, 651. <https://doi.org/10.1007/s12517-020-05673-4>
- Abdelrahman, E. S., & Gobashy, M. (2019). A least-squares minimization approach to interpret gravity anomalies caused by a 2D thick, vertically faulted slab. *Contributions to Geophysics and Geodesy*, 49(3), 229–247.
- Aboelkhair, H., Abdelhalim, A., Hamimi, Z., & Al-Gabali, M. (2020). Reliability of using ASTER data in lithologic mapping and alteration mineral detection of the basement complex of West Berenice, Southeastern Desert Egypt. *Arabian Journal of Geosciences*, 13, 287.
- Aboelkhair, H., Ninomiya, Y., Watanabe, Y., & Sato, I. (2010). Processing and interpretation of ASTER TIR data for mapping of rare-metal-enriched albite granitoids in the Central Eastern Desert of Egypt. *Journal of African Earth Sciences*, 58(1), 141–151.
- Abrams, M., Hook, S., & Ramachandran, B. (2002). ASTER user handbook, version 2. *Jet Propulsion Laboratory*, 4800, 135.
- Abu El-Leil, I., Soliman, N. M. A., Bekiet, M. H., & Elhebiy, M. S. (2019). Enhanced multispectral remote sensing data interpretation for historic gold mines in Egypt: a case study from Madari gold mine. *Arabian Journal of Geosciences*, 12, 3.
- Abu El-Magd, I., Mohy, H., & Basta, F. (2015). Application of remote sensing for gold exploration in the Fawakheir area, Central Eastern Desert of Egypt. *Arabian Journal of Geosciences*, 8, 3523–3536.
- Abuelella, I., Sakran, S., Khalifa, K., & Abdelhalim, A. (2021). Igneous activity around Kharit Basin using remote sensing data analysis, South Eastern Desert. *Egypt. Annals of the Geological Survey of Egypt*, 38, 271–285.
- Aero Service. (1983). Report on calibration tests with the fixed wing gamma-ray spectrometer system. Houston, Texas: Aero service
- Aero Service. (1984a). Compilation procedures to airborne magnetic and radiometric data, prepared for Egyptian general petroleum corporation. Houston, Texas: Aero service
- Aero Service. (1984b). Final operational report of airborne magnetic-radiation survey in the Eastern Desert of Egypt for the Egyptian General Petroleum Corporation. Houston, Texas: Aero service (Six Volumes)
- Akaad, M. K., & Noweir, A. (1980). Geology and lithostratigraphy of the Arabian Desert orogenic belt of Egypt between Lat 25° 35' and 26° 30' N. *Bulletin of Institute for Applied Geology King Abdulaziz University, Jeddah*, 3(4), 127–135.
- Al-Garni, M. A., & Gobashy, M. M. (2010). Ground magnetic investigation of subsurface structures affecting Wadi Thuwal area. *J King Abdulaziz University, JKAU Earth Science.*, 21(2), 167–193. <https://doi.org/10.4197/Ear.21-2.7>
- Amer, R., Kusky, T., & Ghulam, A. (2010). Lithological mapping in the central eastern Desert of Egypt using ASTER data. *Journal of African Earth Sciences*, 56, 75–82.
- Beiki, M., Clark, D. A., Austin, J. R., & Foss, C. A. (2012). Estimating source location using normalized magnetic source strength calculated from magnetic gradient tensor data. *Geophysics*, 77(6), J23–J37. <https://doi.org/10.1190/geo2011-0437.1>
- CONOCO (1987). Geologic map of Egypt (NG 36 SE GabalHammata) scale 1:500,000. Cairo, Egypt: Egyptian GeneralPetroleum Corporation (EGPC). Quseir and Gebel Hamata sheets.
- Dufréchou, G., Harris, L. B., Corriveau, L., & Antonoff, V. (2015). Regional and local controls on mineralization and pluton emplacement in the Bondy gneiss complex, Grenville Province, Canada interpreted from aeromagnetic and gravity data. *Journal of Applied Geophysics*, 116, 192–205.
- Eldosouky, A. M., Sehsah, H., Elkhateeb, S. O., & Pour, A. B. (2020). Integrating aeromagnetic data and Landsat-8 imagery for detecting of post-accretionary shear zones controlling hydrothermal alterations: The Allaqi-Heiani Suture zone, South Eastern Desert. *Egypt. Advances in Space Research*, 65, 1008–1024.
- EldougDoug, A., Abdelazeem, M., Gobashy, M., Abdelwahed, M., Abd El-Rahman, Y., Abdelhalim, A., & Said, S. (2023). Exploring gold mineralization in altered ultramafic rocks in south Abu Marawat, Eastern Desert, Egypt. *Abstract Scientific Reports* 13(1). <https://doi.org/10.1038/s41598-023-33947-w>
- ElGalladi, A., Arafa, S., Mekkawi, M., & Abd-ElHai, M. (2022). Exploring mineralization zones using remote sensing and aeromagnetic data, West Allaqi Area, Eastern-Desert. *Egypt. the Egyptian Journal of Remote Sensing and Space Sciences*, 25, 417–433.
- Elkhateeb, S. O., & Abdellatif, M. A. G. (2018). Delineation potential gold mineralization zones in a part of Central Eastern Desert, Egypt using Airborne Magnetic and Radiometric data. *NRIAG Journal of Astronomy and Geophysics*, 7, 361–376.
- El-Magd, I. A., Mohy, H., & Basta, F. (2014). Application of remote sensing for gold exploration in the Fawakheir area, Central Eastern Desert of Egypt. *Arabian Journal of Geosciences*, 8(6), 3523–3536. <https://doi.org/10.1007/s12517-014-1429-4>
- El-Sawy, E. K., EldougDoug, A., & Gobashy, M. (2018). Geological and geophysical investigations to delineate the subsurface

- extension and the geological setting of Al Ji'lani layered intrusion and its mineralization potentiality, ad Dawadimi district, Kingdom of Saudi Arabia. *Arabian Journal of Geosciences*, *11*(2), 1–25. <https://doi.org/10.1007/s12517-017-3368-3>
- Emam, A., Zoheir, B., & Johnson, P. (2016). ASTER-based mapping of ophiolitic rocks: Examples from the Allaqi-Heiani suture, SE Egypt. *International Geology Review*, *58*, 525–539.
- Gad, S., & Kusky, T. M. (2006). Lithological mapping in the Eastern Desert of Egypt, the Barramiya area, using Landsat thematic mapper (TM). *Journal of African Earth Sciences*, *44*, 196–202.
- Gad, S., & Raef, A. (2012). Factor analysis approach for composited ASTER band ratios and wavelet transform pixel-level image fusion: lithological mapping of the Neoproterozoic Wadi Kid area Sinai Egypt. *International Journal of Remote Sensing*, *33*(5), 1488e1506.
- Gerovska, D., Araúzco-Bravo, M. J., & Stavrev, P. (2004). Determination of the parameters of compact ferro-metallic objects with transforms of magnitude magnetic anomalies. *Journal of Applied Geophysics*, *55*, 173–186.
- Gobashy, M. M., Abbas, E. A. S., Soliman, K. S., & Abdelhalim, A. (2022). Mapping of gold mineralization using an integrated interpretation of geological and geophysical data—a case study from West Baranes, South Eastern Desert. *Egypt. Arab J Geosci*, *15*, 1692. <https://doi.org/10.1007/s12517-022-10955-0>
- Gobashy, M., Abdelazeem, M., & Abdrabou, M. (2020a). Minerals and ore deposits exploration using meta-heuristic-based optimization on magnetic data. *Contributions to Geophysics and Geodesy*, *50*(2), 161–199.
- Gobashy, M., Abdelazeem, M., Abdrabou, M., & Khalil, M. (2020b). Estimating model parameters from self-potential anomaly of 2D inclined sheet using Whale optimization algorithm: Applications to mineral exploration and tracing shear zones. *Natural Resources Research*. <https://doi.org/10.1007/s11053-019-09526-0>
- Gobashy, M. M., Eldougdoug, A., Abdelazeem, M., & Abdelhalim, A. (2021b). Future development of gold mineralization utilizing integrated geology and aeromagnetic techniques: A case study in the barramiya mining District, Central Eastern Desert of Egypt. *Natural Resources Research*, *30*(3), 2007–2028.
- Gobashy, M. M., Metwally, A. M., Abdelazeem, M., Soliman, K. S., & Abdelhalim, A. (2021a). Geophysical exploration of shallow groundwater aquifers in arid regions: A case study of Siwa oasis, Egypt. *Natural Resources Research*, *30*(5), 3355–3384.
- Groves, D. I., Phillips, G. N., Ho S. E., Henderson, C.A., Clark, M. E., & Wood, G.M. (1984). Controls on distribution of Archean hydrothermal gold deposits in Western Australia. In: Foster, R.P. (ed.) *Gold '82 Zimbabwe geol. soc. special publication*, *1*, 689–712.2, 287–322.
- Harraz, H. Z. (2001). A genetic model for a mesothermal Au deposit: Evidence from fluid inclusions and stable isotopic studies at E Sid Gold Mine, Eastern Desert Egypt. *Journal of African Earth Sciences*, *30*, 267–282.
- Harrell, J. A., & Brown, V. M. (1992). The World's oldest surviving geological map: The 1150 B.C. Turin Papyrus from Egypt. *Journal of Geology*, *100*, 3–18.
- Helbig, K. (1963). Some integrals of magnetic anomalies and their relation to the parameters of the disturbing body. *Zeitschrift Für Geophysik*, *29*, 83–96.
- Helmy, H., & Zoheir, B. (2015). Metal and fluid sources in a potential world-class gold deposit: El-Sid mine, Egypt. *International Journal of Earth Sciences*, *104*, 645–661.
- Holden, E.-J., Dentith, M., & Kovesi, P. (2008). Towards the automatic analysis of regional aeromagnetic data to identify regions prospective for gold deposits. *Computers & Geosciences*, *34*, 1505–1513.
- Johnson, P. R., Zoheir, B. A., Ghebreab, W., Stern, R. J., Barrie, C. T., & Hamer, R. D. (2017). Gold-bearing volcanogenic massive sulfides and orogenic-gold deposits in the Nubian Shield. *South African Journal of Geology*, *120*, 63–76.
- Kalinowski, A., & Oliver, S. (2004). ASTER mineral index processing manual. *Remote Sensing Applications, Geoscience Australia*, *37*, 36.
- Klemm, D., Klemm, R., & Murr. (2001). Gold of the Pharaohs - 6000 years of gold mining in Egypt and Nubia. *Journal of African Earth Sciences*, *33*(3–4), 643–659.
- Marquardt, D. W. (1963). An algorithm for least-squares estimation of nonlinear parameters. *Journal of the Society for Industrial and Applied Mathematics*, *11*(2), 431–441.
- Mars, J. C., & Rowan, L. C. (2006). Regional Mapping of Phyllic- and argillic altered rocks in the Zagros Magmatic arc, Iran, Using advanced spaceborne thermal emission and reflection radiometer (ASTER) data and logical operator algorithms. *Geosphere*, *2*, 161–186.
- Miller, H. G., & Singh, V. (1994). Potential field tilt—a new concept for location of potential field sources. *Journal of Applied Geophysics*, *32*(2–3), 213–217.
- Nazih, M., Gobashy, M. M., Salem, Z., Soliman, K. S., & Abdelhalim, A. (2022). Hydrogeochemical and geophysical investigations to delineate underground water aquifer in arid regions: A case study, Gara oasis, Egypt. *Contributions to Geophysics and Geodesy*, *52*(3), 307–357. <https://doi.org/10.31577/congeo.2022.52.3.1>
- Portniaguine, O., & Zhdanov, M. (1999). Focusing geophysical inversion images. *Geophysics*, *64*, 874–887. <https://doi.org/10.1190/1.1444596>
- Qiu, F., Abdelsalam, M., & Thakkar, P. (2006). Spectral analysis of ASTER data covering part of the Neoproterozoic Allaqi-Heiani suture, Southern Egypt. *Journal of African Earth Sciences*, *44*, 169–180.
- Ramadan, T. M., Abdelsalam, M. G., & Stern, R. J. (2001). Mapping gold-bearing massive sulfide deposits in the Neoproterozoic Allaqi suture, southeastern Egypt with Landsat TM and SIR-C/X SAR Images. *Photogrammetric Engineering and Remote Sensing*, *67*, 491–497.
- Rehman, F., Abdelazeem, M., Gobashy, M. M., Harbi, H. M., & Rehman, S. (2019). Application of magnetic method to define the structural setting controlling the contaminated area of Wadi Bani Malik East Jeddah, Saudi Arabia. *Bollettino Di Geofisica Teorica Ed Applicata*, *60*(1), 97–122.
- Reid, A. B., Allsop, J. M., Granser, H., Millet, A. J., & Somerton, I. W. (1990). Magnetic interpretation in three dimensions using Euler deconvolution. *Geophysics*, *55*(1), 80–91.
- Sabins, F. F. (1999). Remote sensing for mineral exploration. *Ore Geology Reviews*, *14*, 157–183.
- Salem, A. M., El Sharkawi, M., El-Alfy, Z., Soliman, N. M., & Ahmed, S. E. (2016). Exploration of gold occurrences in alteration zones at Dungash district, Southeastern Desert of Egypt using ASTER data and geochemical analyses. *Journal of African Earth Sciences*, *117*, 389–400.

- Salem, A., Williams, S., Fairhead, J. D., Ravat, D., & Smith, R. (2007). Tilt-depth method: A simple depth estimation method using first-order magnetic derivatives. *The Leading Edge*, 26(12), 1502–1505.
- Salem, S. M., El Sharkawi, M. A., El Alfay, Z., & Ahmed, S. E. (2018). The use of ASTER data and geochemical analyses for the exploration of gold at Samut area, South Eastern Desert of Egypt. *Arabian Journal of Geosciences*, 11, 541. <https://doi.org/10.1007/s12517-018-3793-y>
- Seleem, T., Hamimi, Z., Zaky, K., & Zoheir, B. (2020). ASTER mapping and geochemical analysis of chromitite bodies in the Abu Dahr ophiolites South Eastern Desert Egypt. *Arabian Journal of Geosciences*. <https://doi.org/10.1007/s12517-020-05624-z>
- Silva, J. B. C. (1986). Reduction to the pole as an inverse problem and its application to low-latitude anomalies. *Geophysics*, 51, 369–382.
- Stavrev, P. (2006). Inversion of elongated magnetic anomalies using magnitude transforms. *Geophysical Prospecting*, 54, 153–166.
- Stavrev, P., & Gerovska, D. (2000). Magnetic field transforms with low sensitivity to the direction of source magnetization and high centricity. *Geophysical Prospecting*, 48, 317–340.
- Thompson D. T. (1982). EULDPH: A new technique for making-computer-assisted depth estimates from magnetic data. *Geophysics*, 47, 31–37.
- Verduzco, B., Fairhead, J. D., Green, C. M., & MacKenzie, C. (2004). New Insights into magnetic derivatives for structural imaging. *The Leading Edge*, 23(2), 116–119. <https://doi.org/10.1190/1.1651454>
- Yang, Y., Li, Y., Deng, X., & Yan, T. (2021). Structural controls on gold mineralization at the eastern margin of the North China Craton: Constraints from gravity and magnetic data from the Liaodong and Jiaodong Peninsulæ. *Ore Geology Reviews*, 139, 104522.
- Zhu, X., & Lu, M. (2021). Fault structures and magmatic intrusions inferred from magnetic data for the Southern Great Xing'an Range, Northern China. *Ore Geology Reviews*, 135, 104206.
- Zoheir, B. A., Creaser, R. A., & Lehmann, B. (2015). Re-Os geochronology of gold mineralization in the Fawakheir area, Eastern Desert Egypt. *Ore Geology Review*, 57, 1418–1432.
- Zoheir, B., Deshesh, F., Broman, C., Pitcairn, A., El-Metwally, A., & Mashaal, S. (2018). Granitoid-associated gold mineralization in Egypt: A case study from the Atalla mine. *Miner Deposita* 53, 701–720. <https://doi.org/10.1007/s00126-017-0772-2>.
- Zoheir, B., Feigenson, M., Zi, J., Deshesh, F., & El-Metwally, A. (2019). Ediacaran (~600 Ma) orogenic gold in Egypt: Age of the Atalla gold mineralization and its geological significance. *Ore Geology Reviews*, 61, 779–794.

(Received November 26, 2022, revised April 4, 2023, accepted April 17, 2023, Published online May 16, 2023)